Domain Walls and Defects in Ferroelectric Inorganic Halide Perovskites $CsGeX_3$ (X = Cl, Br, I)

Kristoffer Eggestad,[1] Benjamin A. D. Williamson,[1] and Sverre M. Selbach[1,*]

[1] *Department of Materials Science and Engineering, NTNU - Norwegian University of Science and Technology, NO-7491 Trondheim, Norway*

(Dated: November 11, 2025)

Among all-inorganic halide perovskites, the only known ferroelectrics are the family of $CsGeX_3$ (X = Cl, Br, I). Here, we study their ferroelectric domain walls (DWs) and common point defects by density functional theory (DFT) calculations and investigate the interplay between DWs and defects. The most stable defects are V_X and V_{Cs} and the former shows low migration barriers and high mobility. In contrast to oxide ferroelectrics, the affinity between point defects and DWs is negligible, reflecting the subtle structural distortions at $CsGeX_3$ DWs. Concomitantly, the formation energies and migration energy barriers of $CsGeX_3$ DWs are small compared to oxides, and neither V_X nor V_{Cs} pin migrating DWs. The band gap invariance across DWs and the lack of affinity towards intrinsic charged point defects imply that conducting DWs for nanoelectronics may be challenging to realise in $CsGeX_3$. However, shallow p-type defect levels and low hole effective masses suggest that high p-type conductivity may be achievable in nominally ferroelectric $CsGeX_3$. The low DW migration energy barriers and insignificant DW pinning by point defects make $CsGeX_3$ promising materials as robust soft ferroelectrics for high-frequency switching applications with low energy dissipation.

I. INTRODUCTION

Halide perovskites have been mostly studied for their optoelectronic and photovoltaic properties [1–4]. Among these, there are also ferroelectric candidates [5, 6], such as the hybrid organic-inorganic compounds with an organic A cation, e.g. MAPI ($CH_3NH_3PbI_3$) [7–9]. Among ferroelectric halide perovskites, the family of $CsGeX_3$ (X = Cl, Br, I) are the only known all-inorganic compounds [10, 11]. The structural ground state is rhombohedral $R3m$, making them isostructural with prototypical perovskite oxides $BaTiO_3$ and $KNbO_3$ [12–17], and different from MAPI which is typically reported as tetragonal at room temperature [18]. They possess T_C s of 155°C, 238°C, and 277°C for X = Cl, Br, I [19], respectively, and polarisations [10] within $10 - 20$ μC/cm^2. Most studies hitherto of $CsGeX_3$ have emphasised photovoltaic properties, including several *ab initio* studies of the electronic structure [20–25]. $CsGeCl_3$ has also shown promise as a p-type conductor, similar to Sn(II)O, where traditionally localised deep lying holes situated on O $2p$ (in Sn(IV)O_2, an n-type conductor) are now delocalised thanks to covalency between O $2p$ and Ge $4s$, lowering the effective mass of holes and the ionisation potential allowing for low formation energy shallow defects such as V_{Cs} [26, 27]. The related $CsSnX_3$ and $CsPbX_3$ also possess B-site lone pairs, but here tensile strain is needed to stabilise polarisation [28].

Conductive ferroelectric DWs were first reported in La-doped $BiFeO_3$ [29], but have later been shown in a multitude of materials systems [30–32]. DWs in ferroelectric and ferroelastic oxides are known to become conducting [30, 33] from either intrinsic effects such as band bending at neutral or charged DWs [29, 34–36], or by extrinsic effects such as electronic charge compensation of charged point defects accumulating at the DWs [37–39]. The space group of $CsGeX_3$, $R3m$, allows 71°, 109° and 180° ferroelectric DWs. The 71° and 109° DWs must also be ferroelastic as the strain state changes across these walls. Our study of DWs in $CsGeX_3$ is also motivated by the high charge carrier mobility [40, 41], defect tolerance [41–45] and intermediate band semiconductivity [46, 47], all implying that different physical DW properties compared to oxides are anticipated.

Here, we use density functional theory (DFT) calculations to study DWs and point defects in ferroelectric $CsGeX_3$ (X = Cl, Br, I). We calculate electronic structure, DW mobility, point defect formation energies and migration barriers, and interactions between DWs and point defects. $CsGeX_3$ exhibit significantly different DW energies, mobilities, and electronic structures compared to corresponding oxides. High DW mobility, point defect insensitivity, and propensity to p-type doping give the all-inorganic halide perovskites a distinctly complementary technological potential compared to oxide ferroelectrics.

II. COMPUTATIONAL DETAILS

Point defects and DWs in $CsGeX_3$ have been investigated using density functional theory (DFT) within the `VASP` code [48–50]. Interactions between core and valence electrons (Cs: ($4s^2$, $4p^6$, $5s^1$), Ge: ($3d^{10}$, $4s^2$, $4p^2$), Cl: ($3s^2$, $3p^5$), Br: ($4s^2$, $4p^5$), I: ($5s^2$, $5p^5$)) were treated using the projector-augmented-wave method (PAW) [51, 52]. The HSE06 functional [53] (Heyd-Scuseria-Ernzerhof screened hybrid functional, with mixing parameter $\alpha = 0.25$ and screening parameter $\omega = 0.11$ bohr^{-1}) was used for all bulk structure calculations, as it yields lattice parameters in close agreement with experimental values (see Table I) and is known to provide accurate descriptions of electronic structure and carrier localisation [54, 55]. Due to the high computational cost of HSE06, the PBEsol [56] functional

* selbach@ntnu.no

(Perdew-Burke-Ernzerhof revised for solids) was used to investigate defect mobilities and domain walls. A plane-wave energy cutoff of 400 eV was used for all calculations. The effects of spin-orbit coupling (SOC) were studied for all three halide systems, however, only minor changes in the electronic structure of $CsGeI_3$ were observed (see SI Figure S5), and thus SOC was omitted in subsequent calculations to reduce computational cost.

Electronic density of states (DOS) were calculated using primitive cells containing 5 atoms. Geometries and atomic positions were optimised until all forces on all ions were less than 1×10^{-4} eV^{-1} using $8 \times 8 \times 8$ Γ-centred *k*-point meshes. *k*-points along high-symmetry paths, for electronic band structure calculations, were generated using the `SUMO` program [57].

Polarisation was estimated using the point charge model, with formal charges (FC) and Born effective charges (BEC), and the Berry phase method. BEC were calculated using finite differences and tabulated in SI Table S6. The finite differences method also gives elastic, piezoelectric and dielectric tensors, presented in SI Table S6, S7, S8 and S9. Similar properties have been estimated using density functional perturbation theory (DFPT) with the PBEsol functional and are displayed in SI Table S11, S12, S13 and S14. Intrinsic point defect formation energies were calculated using [58]

$$\begin{aligned}\Delta H_F(D,q) =& E_{\mathrm{D}}(q) - E_{\mathrm{H}} + \sum_i n_i(E_i + \mu_i) \\ &+ q(E_{\mathrm{F}} + E_{\mathrm{vbm}} + E_{\mathrm{corr}}^{\mathrm{pot}}) + E_{\mathrm{corr}}^{\mathrm{IC}} + E_{\mathrm{corr}}^{\mathrm{BF}}\end{aligned} \tag{1}$$

where E_{H} is the reference energy of the pristine host cell. $E_{\mathrm{D}}(q)$ is the energy of the supercell including the defect, D, with charge state q. E_i and μ_i are the reference energy and the chemical potential of element i, respectively, and n_i is the number of element i removed from the system. E_{F} is the Fermi level for which to evaluate the defect formation energies, while E_{VBM} refers this energy to the energy of the valence band maximum in the DFT calculations. Due to the limited supercell, three correction schemes, $E_{\mathrm{corr}}^{\mathrm{pot}}$, $E_{\mathrm{corr}}^{\mathrm{IC}}$ and E_{corr}^{BF}, are employed to correct for finite size effects. The potential alignment correction, $E_{\mathrm{corr}}^{\mathrm{pot}}$, aligns the potential of the defect cell to that of the defect free host cell [59], and the image charge correction, $E_{\mathrm{corr}}^{\mathrm{IC}}$, corrects for the interactions between the defect and the charge of its periodic image [59, 60]. Lastly, the band filling correction, E_{corr}^{BF}, corrects for the unphysical filling of holes and electrons in the valence and conduction band, respectively [59, 61].

The thermodynamic stability regions of $CsGeCl_3$ and $CsGeI_3$, shown in SI Figure S6 and S7, are calculated by evaluating formation energies of all competing phases using the Chemical Potential Limits Analysis Program (`CPLAP`) [62]. To show the full defect chemistry of $CsGeCl_3$ and $CsGeI_3$, defect formation energies, shown in Figure 4 a and b, are calculated using three sets of chemical potentials for both materials, indicated in SI Figure S6 and S7.

The mobility of V_{Cs} and V_X were investigated using the climbing image nudged elastic bands method [63, 64] (ci-NEB) with 5 images between the initial and final image. The migration barriers were calculated in both supercells with and without charge compensation. Two different migration paths for V_X, displayed in SI Figure S9, were investigated.

Lattice parameters for 71°, 109° and 180° DW cells for $CsGeX_3$ were calculated from the equations displayed in SI Table S15 using the PBEsol optimised lattice parameters. To avoid DW-DW interactions, a-parameters of ~ 75 Å were used. Γ-centred *k*-point meshes of $1 \times 4 \times 6$, $1 \times 4 \times 4$, $1 \times 6 \times 4$ and $1 \times 6 \times 4$ were used for the for 71°, 109° and 180° Y- and X-type DW supercells, respectively. The atomic positions were relaxed until all forces on all ions were less than 0.001 eV Å^{-1}. DW supercells, for $CsGeCl_3$, with DFT optimised atomic positions are shown in SI Figure S11.

Investigations of defect segregation enthalpies were investigated by calculating the defect formation energies as a function of distance from a 71° DW in $CsGeCl_3$. To avoid defect-defect interactions the cross section area of the DW supercells was increased by an $1 \times 2 \times 3$ expansion and a Γ-centred *k*-point mesh of $1 \times 2 \times 2$ was used.

The mobility of DWs was investigated using the ci-NEB method with 5 images. A strict force criterion of 0.001 eV Å^{-1} was used for optimising the atomic positions of the start and end images due to the flat energy landscape around the DW equilibrium position. ci-NEB calculations were performed with a force criterion of 0.01 eV Å^{-1}. Point defect pinning was studied for 71° DWs in $CsGeCl_3$ by calculating migration barriers across point defects in DW supercells. The supercells used are described in SI Table S16 and Figure S17 and a Γ-centred *k*-point mesh of $1 \times 2 \times 2$ and a force criterion of 0.01 eV Å^{-1} was used for structure optimisation.

III. RESULTS

The structural properties of the relaxed primitive cells, see Figure 1, were calculated and are presented in Table I. Our calculated lattice parameters show good agreement with experimental values reported in the literature [11, 19, 65, 66]. The HSE06 functional gives excellent agreement with experiments, with a subtle overestimation, as expected due to thermal expansion and related effects. Estimated polarisation using formal charges (FC), Born effective charges (BEC) and Berry phase calculations are shown in Table II and show a decreasing polarisation from $CsGeCl_3$ to $CsGeI_3$. The Berry phase method suggests significantly larger polarisations than using BEC and the point charge model, indicating significant contribution from electrons. Our values are relatively close to what has been reported previously using the PBE functional [10].

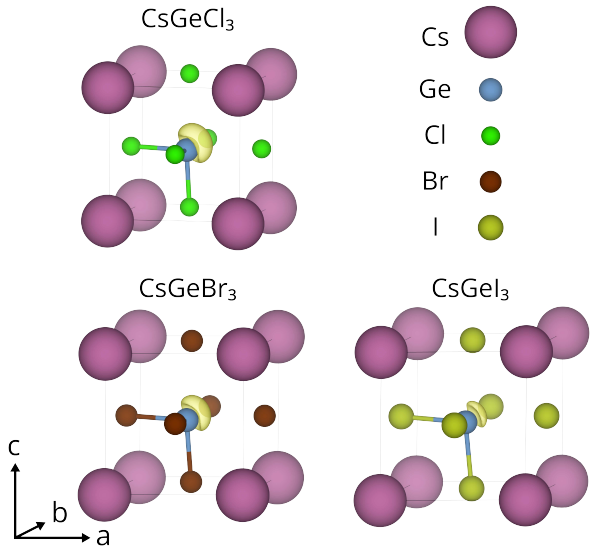

FIG. 1. DFT optimised primitive structures of $CsGeCl_3$, $CsGeBr_3$ and $CsGeI_3$ visualised together with their respective lone pairs. The lone pairs are extracted from the partial charge density of the top valence bands and shown with an isosurface level of 0.02.

TABLE I. Calculated and experimental lattice parameters and Ge-X bond lengths for the primitive unit cell of $CsGeCl_3$, $CsGeBr_3$ and $CsGeI_3$. The bonds described are the bonds shown in Figure 1.

		PBE	PBEsol	HSE06	Exp.
$CsGeCl_3$	a,b,c (Å)	5.519	5.294	5.513	5.444[11], 5.434[19], 5.391[66]
	α,β,γ (°)	89.00	89.76	89.49	89.63[11], 89.72[19], 89.71[66]
	Ge-Cl (Å)	2.41	2.42	2.37	2.35 [19]
$CsGeBr_3$	a,b,c (Å)	5.744	5.504	5.731	5.636[19, 65], 5.638[66]
	α,β,γ (°)	88.45	89.53	88.46	88.74[19, 65], 88.73[66]
	Ge-Br (Å)	2.58	2.60	2.54	2.53 [19]
$CsGeI_3$	a,b,c (Å)	6.108	5.860	6.081	5.983 [19]
	α,β,γ (°)	88.25	89.49	88.14	88.61 [19]
	Ge-I (Å)	2.79	2.80	2.75	2.75 [19]

A. Electronic Structure

Partial and total electronic density of states (DOS) are calculated for $CsGeX_3$ and displayed in Figure 2. The conduction band minimum (CBM) consist mainly of Ge p states with some covalency with X p. The valence band maximum (VBM) show mixing of Ge s, Ge p and X p. The Ge lone pair can be seen at the top of the valence band as hybridisation between Ge s and Ge p. The lone pair causes an off-centring of the Ge ions and thus non-centrosymmetry and ferroelectricity in these halide perovskites.

The strength (stereochemical activity) of the lone pair can be determined by the overlap between Ge s and X p as good overlap results in mainly non-bonding Ge s states that are high enough in energy for hybridisation with Ge p. The overlap between Ge s and X p and the lone pair are shown in detail in SI Figure S4. The degree of covalency between Ge s and X p has been quantified by calculating the X p contribution to the covalency between Ge s and X p at around -9 eV in a similar fashion as what was done by Payne et al. for a series of post-transition metal oxides [67, 68]. Calculated X p contribution of 0.34, 0.25 and 0.17 for $CsGeCl_3$, $CsGeBr_3$ and $CsGeI_3$, respectively, predicts stronger mixing and thus stronger lone pairs going from $CsGeI_3$ to $CsGeCl_3$. The energy of X p increases down the periodic table leading to less mixing of Ge s and X p, therefore weaker hybridisation between Ge s and Ge p, and a weaker lone pair. The evaluated lone pair strength correlates nicely with decreasing band gaps and polarisation from $CsGeCl_3$ to $CsGeI_3$. DOS-es calculated using the PBEsol functional show very similar trends and are displayed in SI Figure S3. To further illustrate the nature of the lone pairs, Figure 1 show the real-space projections of the charge density at the top of the valence band.

TABLE II. Tolerance factor, polarisation, band gaps and effective masses of holes and electrons calculated for $CsGeX_3$ (X = Cl, Br, I) using the HSE06 functional. Born effective charges are calculated using the finite differences method.

	$CsGeCl_3$	$CsGeBr_3$	$CsGeI_3$
t	1.027	1.009	0.985
P_{FC} (μC/cm^2)	8.5	7.6	6.9
P_{BEC} (μC/cm^2)	10.84	10.47	9.88
P_{Berry} (μC/cm^2)	24.3	21.3	21.0
E_g (eV)	3.015	2.068	1.438
m_h^*	0.325	0.189	0.138
m_e^*	0.438	0.187	0.134

Calculated band structures show direct band gaps at Z of $\sim$ 3.0, 2.1 and 1.4 eV, slightly lower than experimental values reported for $CsGeCl_3$ and $CsGeBr_3$ [46]. From $CsGeCl_3$ to $CsGeI_3$, both the lattice parameters and Ge-X bond lengths increase, which is inversely correlated with the observed reduction in band gap. Moreover, calculated band structures show a large degree of curvature at the band edges and display large band gaps of around 4 eV at the Γ point demonstrating the importance of the k-point sampling [69]. Calculated effective masses, displayed in Table II, show exceptionally low effective masses. According to the classification by Davies et al. [70], which characterises the degree of polaronic behaviour, $CsGeCl_3$ lies on the border between type I and II, while $CsGeBr_3$ and $CsGeI_3$ fall firmly within type I. Therefore, very high electron and hole mobilities are expected for $CsGeBr_3$ and $CsGeI_3$, whereas some degree of polaronic behaviour is expected in $CsGeCl_3$. The PBEsol functional gives relatively similar band structures, see SI Figure S3, albeit significantly lower band gaps. The bottom two bands of the CB are al-

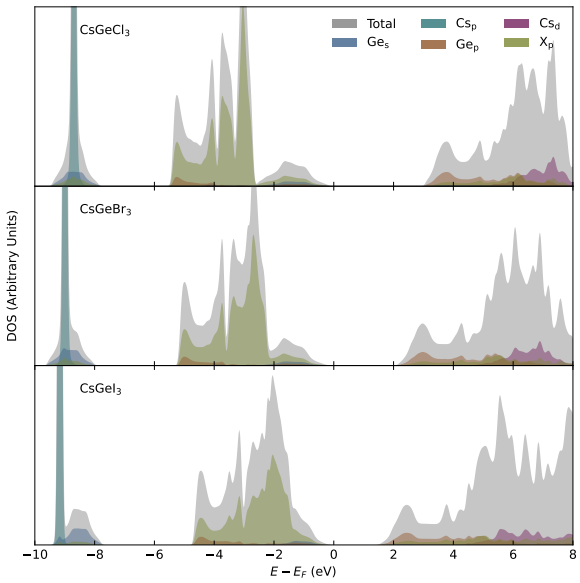

FIG. 2. Electronic density of states for $CsGeCl_3$, $CsGeBr_3$ and $CsGeI_3$ calculated using the HSE06 functional. Cs p, Cs d, Ge s, Ge p and X p (halogen-p) are shown and coloured in turquoise, purple, blue, orange and green, respectively. Other orbitals do not contribute significantly and are thus omitted.

most degenerate at the F and Z points in $CsGeCl_3$, but less so in $CsGeBr_3$ and $CsGeI_3$. The localised bands at around -9 eV are Cs p as seen in the DOS in Figure 2.

B. Intrinsic Defect Thermodynamics

Defect formation energies as a function of the Fermi energy for $CsGeCl_3$ and $CsGeI_3$, calculated using the HSE06 functional, are displayed in Figure 4 a and b. Each figure includes three panels showing the formation energies at three different parts of the stability window, indicated in SI Figure S6 and S7. Hybrid defect calculations were not performed for $CsGeBr_3$, as this compound is expected to exhibit intermediate properties between $CsGeCl_3$ and $CsGeI_3$.

Throughout the stability region, the defects with the lowest formation energies are V_{Cs}, V_{Ge}, and V_X. Halide interstitials show relatively high formation energies, and therefore, V_X are expected to be the dominant halide defects. Moreover, cation antisites also show high formation energies, due to the difference in charge and size (0.73 Å, 1.88 Å[71]) between Cs and Ge ions.

All n-type defects show deep transition levels while several p-type defects display shallow or resonant defect levels. V_{Cs} show shallow defect levels (-1/0) of 0.004 and 0.015 eV above the VBM in $CsGeCl_3$ and $CsGeI_3$, respectively, while V_{Ge} is deep in $CsGeCl_3$ and resonant in $CsGeI_3$. At the halogen rich limit (left panels), the Fermi level is pinned at approximately 0.4 and 0.07 eV above the VBM for $CsGeCl_3$ and $CsGeI_3$, respectively. Both materials show p-type dopeability at this part of the stability region. Towards the halogen poor edge, the Fermi level shifts towards the middle of the band gap and less p-type character is observed.

Point defects and p-type conductivity in $CsGeCl_3$ have previously been investigated, using DFT with the PBE functional, by Huang et al.[27]. Despite the different functional, our calculations show similar results to what they report, but as expected, the HSE06 functional gives deeper transition levels as HSE06 is known to better localise holes and electrons. Using the HSE06 functional also results in subtly larger formation energies on average.

Calculated migration barriers for V_{Cs} and V_{Cl} in both neutral and charged supercells of $CsGeCl_3$ are displayed in Figure 5. V_{Cs} show relatively low migration barriers of $\sim$ 0.75 eV, while V_{Cl} display very low migration barriers comparable with V_{Li} and V_{Na} in the best solid state batteries [72, 73]. In the charged cell, without any charge compensation, the migration barriers are $\sim$ 0.22 eV and $\sim$ 0.24 eV, and in the charged cell, compensated by one extra electron, $\sim$ 0.30 eV and $\sim$ 0.33 eV for path I and II, respectively. Path I is between two Cl sites with their short Ge-Cl bonds to the same Ge atom while path II is between two Cl sites with their short bonds to two different Ge atoms. Both paths are displayed in SI Figure S9. Migration of charge compensated V_{Cl} through path II shows an additional small barrier due to polaron hopping.

V_{Cs} and V_I in $CsGeI_3$ show very similar migration barriers to what is shown for $CsGeCl_3$, see SI Figure S8. Mobile ions are known as one of the main contributors to the degradation of halide perovskite solar cells [74, 75], however, for instance, calculated migration barrier for V_I in methylammonium lead iodide ($CH_3NH_3PbI_3$) of 0.6 eV [76] is significantly higher than what is estimated in this work.

C. Domain Walls

Calculated DW energies, summarised in Table III, indicate that 71° DWs are the most favourable type in $CsGeX_3$, closely followed by 109° DWs. Both exhibit minimal structural distortion and form narrow walls, as illustrated in SI Figures S12, S13, and S14 for $CsGeCl_3$, $CsGeBr_3$, and $CsGeI_3$, respectively. In contrast, 180° DWs induce significant lattice distortions, resulting in substantially higher DW energies. Notably, the energies of 71° and 109° DWs in $CsGeX_3$ are considerably lower than those reported for most ferroelectric oxide perovskites. For comparison, reported DW energies for 180° DWs in $LiNbO_3$, 109° DWs in $BiFeO_3$, 90° DWs in $PbTiO_3$, 90° DWs in orthorhombic $KNbO_3$, and 71° and 109° DWs in $BaTiO_3$ are 141[77], 33[78], 35[79], 4.3[80], 3.8[81] and 11.1[81] mJ/m^2, respectively. In contrast, DW energies reported for the metal-organic halide perovskite $MAPX_3$ (X = Cl, Br, I) are 3, 1, and 8 mJ/m^2 [82], respectively, which are comparable to those found in this study.

As there are very little distortions associated with the low-energy DWs, there are almost no changes to the interatomic distances and bonding, and therefore almost no

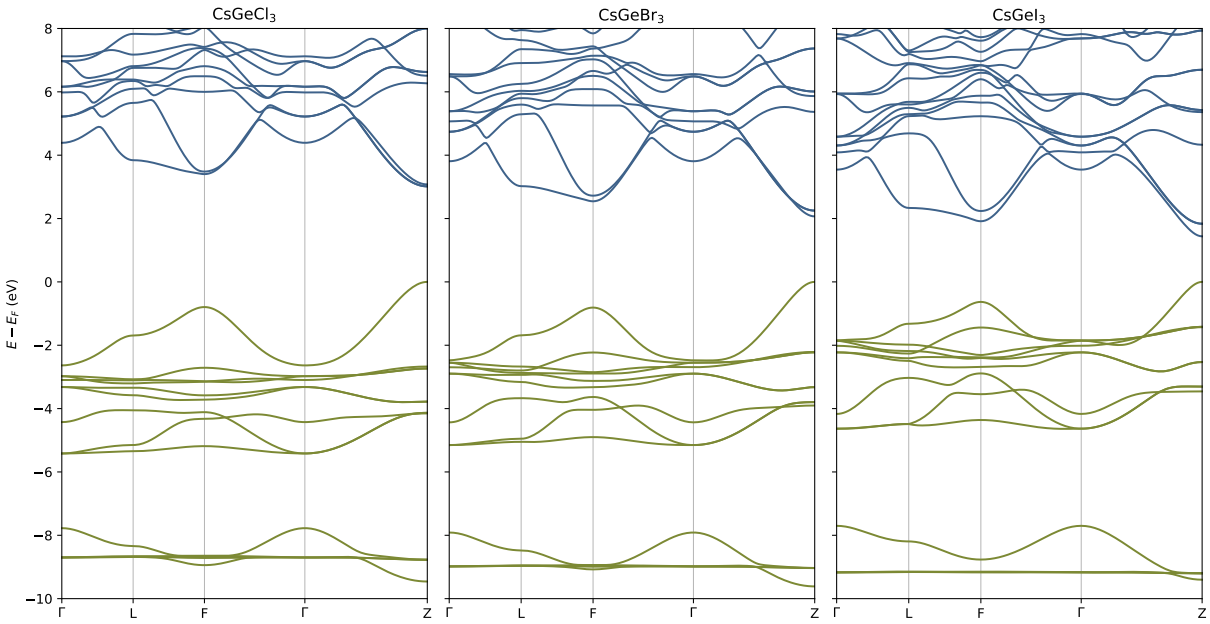

FIG. 3. Electronic band structures for $CsGeCl_3$, $CsGeBr_3$ and $CsGeI_3$ calculated using the HSE06 functional. The valence and conduction band are coloured in green and blue, respectively.

TABLE III. Calculated domain wall energies for DWs in $CsGeCl_3$, $CsGeBr_3$ and $CsGeI_3$ calculated using the PBEsol functional.

DW-type	$CsGeCl_3$ (mJ/m^2)	$CsGeBr_3$ (mJ/m^2)	$CsGeI_3$ (mJ/m^2)
71°	1.6	1.1	1.5
109°	1.7	4.2	2.5
180° Y	47	18	19
180° X	57	22	21

changes in the electronic structure are observed at the DWs, see SI Figure S15. Therefore, no reduction in bandgap at the DWs in $CsGeX_3$ is expected and also not observed.

D. Interactions Between Point Defects and Domain Walls

The 71° DWs in $CsGeCl_3$ were selected as the model system for investigating interactions between point defects and DWs, in order to reduce both complexity and computational cost. Given the similar behaviour of point defects (Figure 4, 5 and SI Figure S8) and DWs (Table III, SI Figure S12, S13 and S14) across these compounds, the interactions between point defects and DWs are also expected to be comparable. Moreover, as $CsGeCl_3$ exhibits larger structural distortions, higher polarisation, stronger lone pair activity, and more pronounced polaronic behaviour, the interactions between point defects and DWs in $CsGeCl_3$ is expected to be more significant than in the other compounds. The 71° DW was chosen because it has the lowest formation energy for the compounds considered, making it the most likely to form.

SI Figure S16 shows normalised defect formation energies as a function of distance from a 71° DW in $CsGeCl_3$. The energies are normalised to the defect formation of the same defect at the centre of one of the domains. None of the investigated point defects show any significant change in formation energy at DWs compared to domain centres or bulk. V_{Ge} show the largest reduction in energy at the DW, but this is only a reduction of $\sim$0.005 eV, which is below the thermal energy (k_BT) at room temperature. Both V_{Cs} and V_{Ge} show a weak increase in energy approaching the DW before it decreases at the DW. However, these changes are very small and not likely to have any experimental significance.

Point defects typically exhibit reduced defect formation energies at DWs, due to the inherent strain fields and distortions associated with the DWs [38, 77, 83, 84]. Generally, point defects accumulate at DWs to maximise the volume of unperturbed bulk material, under the condition that the local structural distortions caused by DWs and the point defects are compatible [83, 85]. However, as there are very little distortions accompanying the low-energy DWs in $CsGeX_3$, almost no change in defect formation energies is observed at the 71° DWs in $CsGeCl_3$.

Migration barriers for 71° DWs in $CsGeCl_3$, $CsGeBr_3$ and $CsGeI_3$ without point defects are displayed in Figure 7. The figure shows very low migration barriers for 71° DWs, with migration barriers of $\sim$ 5.4, 1.0 and 0.7 mJ/m^2 for $CsGeCl_3$, $CsGeBr_3$ and $CsGeI_3$, respectively. These are all significantly lower than values reported for ferroelectric oxides, where, for example, 180° DWs in h-$YMnO_3$ $LiNbO_3$, and $PbTiO_3$ are reported with migration barriers of $\sim$30[83, 86], 35[77] and 37[79] mJ/m^2. $CsGeCl_3$ show a migration barrier larger than the energy required to form the DW. Cal-

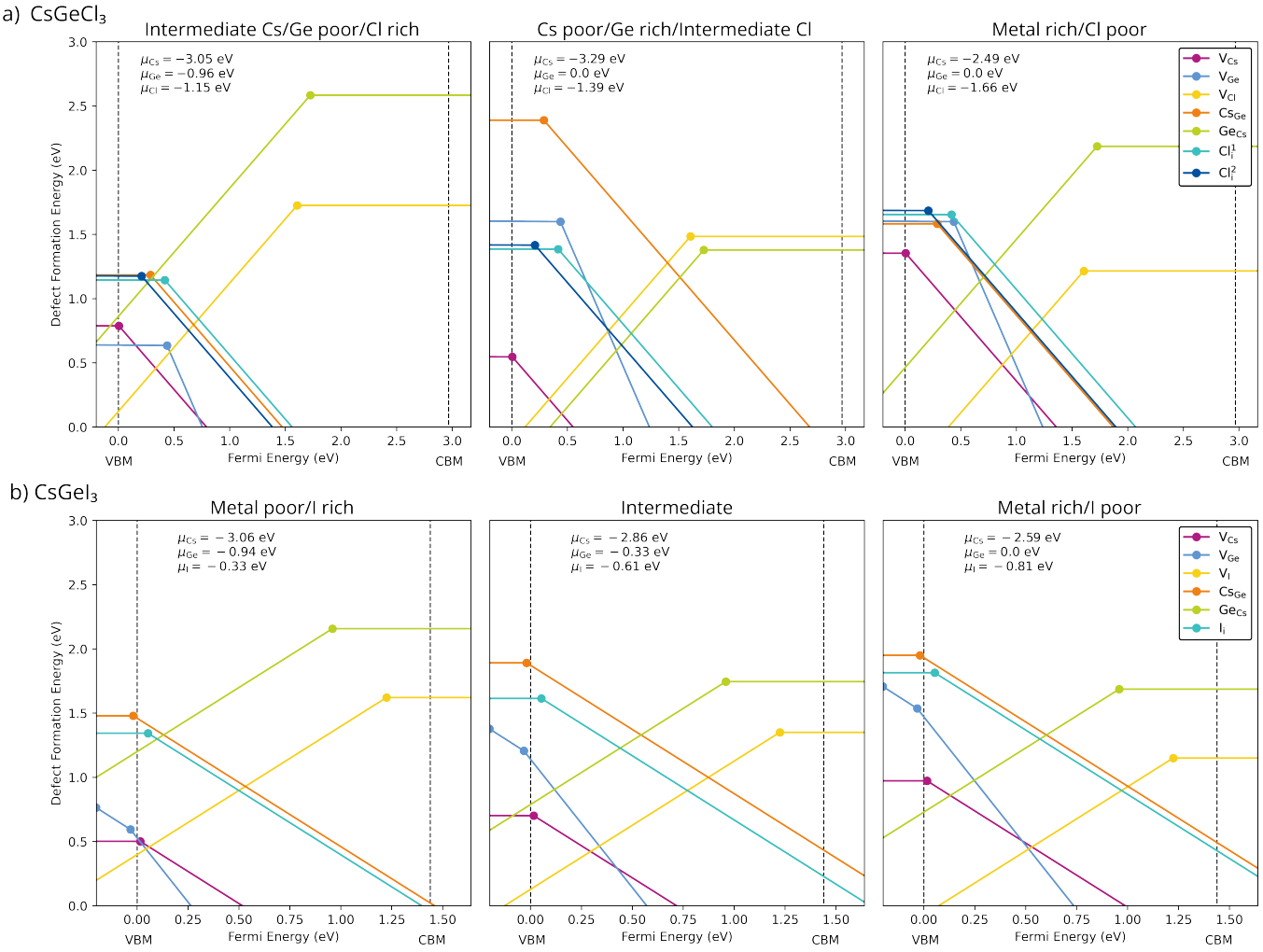

FIG. 4. Thermodynamic transition level diagrams for intrinsic defects in bulk $CsGeCl_3$ (a) and $CsGeI_3$ (b) calculated using the HSE06 functional. The three panels for each compound show the transition levels at three different chemical environments indicated in the stability window shown in SI Figure S6 and S7. The dashed lines at 0 eV, and ~ 3 and ~ 1.5 eV display the VBM and CBM, respectively.

culating the migration barriers of 109° DWs was also attempted, but while "moving", each DW just transforms into two 71° DWs. The weak interaction between DWs and point defects is also reflected in the calculated DW migration barriers shown in Figure 8. The figure shows calculated migration barriers for a 71° DW in $CsGeCl_3$ with and without point defects in the supercell. The position of the defects is indicated by the filled circles and the DWs are moved in two steps. First approaching the defect, then moving past it. The interactions between the DW and defects are investigated using neutral and charged cells. The point defects studied are V_{Cs}, V_{Ge} and in-plane and out-of-plane V_{Cl} as well as V_{Cs} + V_{Cl} defect pairs.

V_{Cs} results in an increased migration barrier of almost 40 %, however, the migration barriers are still very small. There is also a subtle increase in the migration barrier for the DW moving to the defect. Additionally, introducing a compensating hole into the system does not alter the results.

Also, for V_{Ge} there is no significant difference between calculations performed with or without hole compensation. V_{Ge} does not result in any increase in migration barriers, but, as seen in the figure, the DW prefers to be situated where the defect is located. A small reduction in the total energy is also observed, similar to what is shown in SI Figure S16, when the DW coincides with the position of the V_{Ge}.

The two inequivalent V_{Cl} affect the DW very differently. An in-plane V_{Cl} compensated by an electron leads to a substantial increase of the migration barrier of about 400%. In contrast, when the in-plane V_{Cl} is not compensated by an electron, the DW prefers to be co-located with the defect. For the out-of-plane V_{Cl}, there is no change in the migration barrier if the defect is not charge-compensated, while charge compensation results in a similar increase in the migration barrier as observed for V_{Cs}.

During the movement of a 71° domain wall, one in-plane Ge-Cl bond is formed while another bond is broken. If a

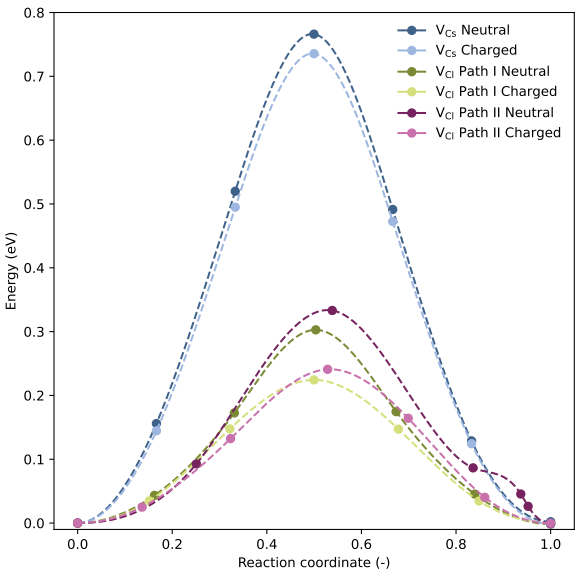

FIG. 5. Migration barriers of V_{Cs} and V_{Cl} in bulk $CsGeCl_3$ in charged and neutral cells calculated using the PBEsol functional.

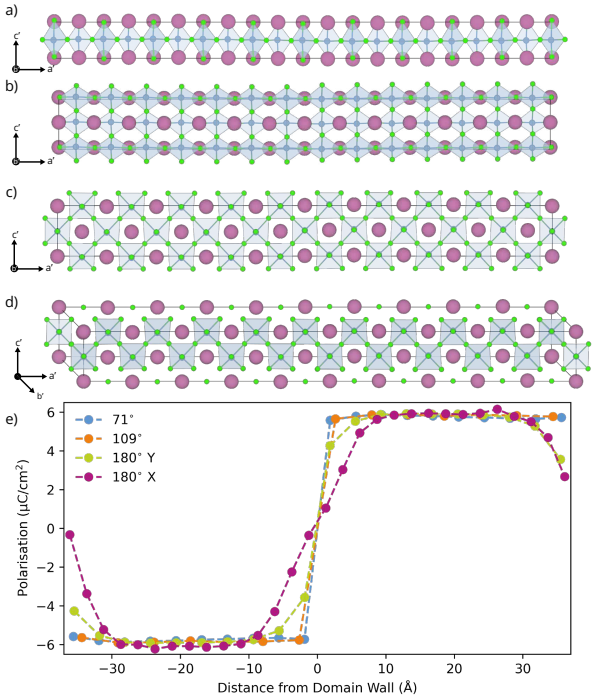

FIG. 6. PBEsol optimised 71° (a), 109° (b), 180° Y-type (c) and 180° X-type (d) ferroelectric domain walls in $CsGeCl_3$. Estimated polarisations, from formal charges using the point charge model, are displayed in (e) as a function of the supercell dimension perpendicular to the domain walls. The relation between the supercells' and primitive cells lattice parameters is shown in SI Table S15.

charge-compensated in-plane V_{Cl} is present at the domain wall, the polaron that compensates the defect must also transfer from one Ge atom to another, explaining the substantially increased migration barrier resulting from this specific point defect.

The investigated defect clusters show combined characteristics of the individual defects in the charged unit cells. V_{Cs} together with in-plane V_{Cl} show increased migration barriers, similar to V_{Cs}, and a preference for the in-plane V_{Cl}. V_{Cs} together with out-of-plane V_{Cl} show increased migration barriers relatively similar to just a combination of the increased migration barriers of the individual defects.

IV. DISCUSSION

The potential of $CsGeCl_3$ as a transparent p-type conductor has previously been discussed in work by Huang et al. [27], who highlighted its high hole mobility as well as favourable formation energy and transition level of p-type V_{Ge}. Our hybrid functional calculations support their findings regarding the high hole mobility and low formation energy of V_{Ge}. However, using the HSE06 functional, we find that V_{Ge} exhibits a significantly deeper transition level than previously reported (~ 0.5 eV) [27]. In contrast, V_{Cs} displays both a shallow transition level and low formation energy. For $CsGeI_3$, both V_{Cs} and V_{Ge} show low formation energies, shallow transition levels, and even lower hole effective masses. These results indicate that both materials are promising candidates for p-type conductivity. Additionally, at specific chemical environments the energy of n-type defects, namely V_X, is sufficiently high that the introduction of a good p-type dopant can pin the Fermi level within the valence band. Regarding transparent conductivity, $CsGeCl_3$ show a band gap close to the energy of visible light, and has been reported experimentally with an even larger band gap [87] as well as forming colourless crystals [11].

Calculated migration barriers for V_{Cl} and 71° DWs over V_{Cl} in neutral cells show larger migration barriers than migration barriers calculated using charged cells. This means that the extra charge compensating electron in neutral cells affects both the mobility of halogen vacancies as well as the DW mobility. This is likely due to the charge-compensating electrons populating anti-bonding Ge p states, destabilising the lone pair. In the charged cells without charge-compensating electrons, the lone pair is able to rotate more freely about its parent Ge ion and we hypothesise that this helps stabilising V_{Cl} in the intermediate states, thus reducing the energy of the transition state.

Furthermore, both V_{Cl} migration through path II and DW migration past an in-plane V_{Cl} in neutral cells, require electron transfer between two Ge atoms (see SI Figure S10). In $CsGeCl_3$, the deep transition level of V_{Cl} suggests an electron transfer through polaron hopping. The migration barrier associated with the polaron hopping will add to the total migration barrier, which explains the increased energy barriers of these migrations.

In contrast, in $CsGeI_3$, there is no difference in V_I migration barriers for the different paths (SI Figure S8). V_I shows a significantly more shallow defect level than V_{Cl} and using

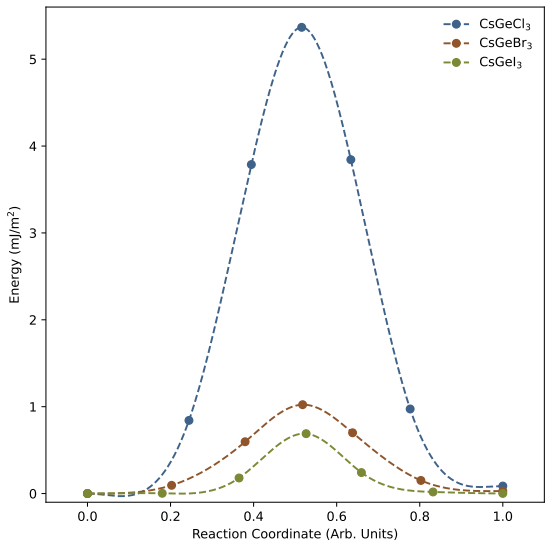

FIG. 7. Calculated migration barriers for 71° DWs in $CsGeCl_3$, $CsGeBr_3$ and $CsGeI_3$ using the PBEsol functional and the ci-NEB method.

PBEsol, the compensating electron is predominantly delocalised and thus no increase in migration barrier for path II is observed. Ultimately, calculations with charge compensation by electrons are likely not important as these materials show a strong p-type character and V_{Cl} will instead be compensated by other defects rather than electrons.

DWs in $CsGeX_3$ show low formation energies, as well as low migration barriers. However, because of the subtlety of the structural distortions across the DWs, no significant change in point defect formation energy or electronic structure is observed at the DW. It is therefore likely difficult to obtain exotic electronic properties at the DWs of these materials. Despite the low defect formation energies, shallow transition levels, low defect migration barriers, and good carrier mobilities, this means that $CsGeX_3$ are not promising candidates for DW-based electronics.

Instead, low DW migration barriers indicate low energy loss and joule heating during polarisation reversal, and are thus useful for applications where high switching frequencies are needed, e.g. for FeRAMs, GHz transducers, and electro-optics.

V. CONCLUSION

Using hybrid functional DFT we have found that ferroelectric inorganic halides $CsGeX_3$ show highly mobile electrons and holes. The point defects V_{Cs} and V_X show low formation energies and low and very low, respectively, migration energy barriers. This implies that point defects should be very important to the functional properties of these materials. Furthermore, low formation energy p-type defects show shallow defect levels and there is a potential for p-type doping of this ferroelectric material with an electronic band gap almost large enough to make it transparent to visible light.

We have shown that 71° exhibit very low formation energies, closely followed by 109° DWs. This is a consequence of the very subtle structural distortions found at these DWs compared to bulk, in contrast to the pronounced distortions often observed in oxide ferroelectrics. The absence of significant strain fields means that point defects show little tendency to accumulate at the DWs, and the electronic structure closely resembles that of the bulk. Consequently, $CsGeX_3$ is unlikely to be suitable for DW-based electronics.

However, the low formation energy of the DWs, and especially the remarkably high mobility of 71° DWs, make $CsGeX_3$ materials promising candidates for applications as ferroelectrics that require high-frequency switching with low energy dissipation. The insensitivity to point defects and the inclination towards p-type doping emphasises the different properties and technological potential of ferroelectric halide perovskites compared to oxide perovskites.

VI. ACKNOWLEDGEMENTS

Financial support for this project was provided from the Research Council of Norway through projects no. 302506, 301954, and 354614. Computational resources were provided through project no. NN9264K at Sigma 2 the National Infrastructure for High-Performance Computing and Data Storage in Norway.

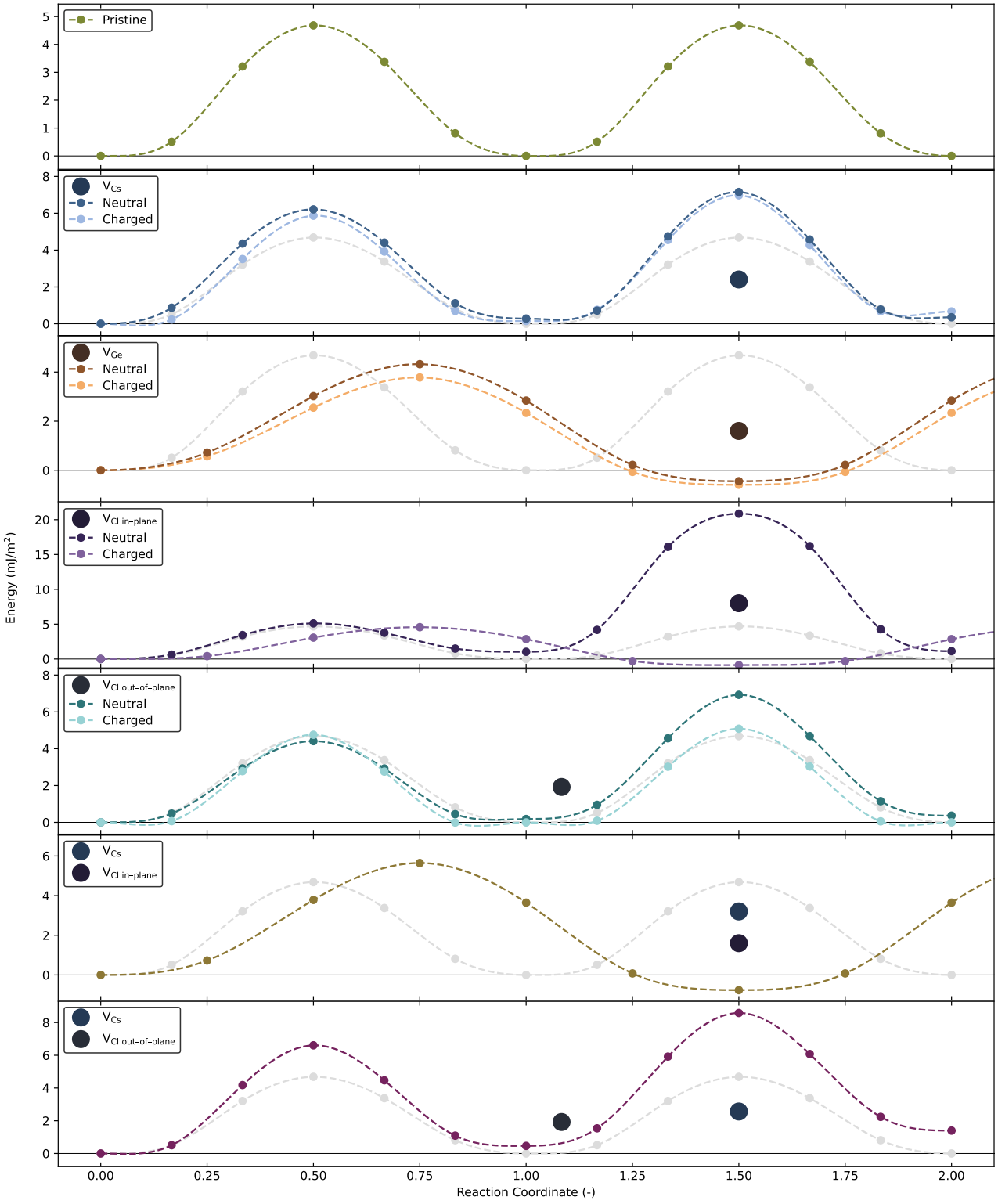

FIG. 8. DW migration barriers for 71° DWs in $CsGeCl_3$ with and without defects in its vicinity. The first plot shows the migration barrier in the pristine DW cell. The next four plots show migration barriers in cells with V_{Cs}, V_{Ge}, V_{Cl} and V_{Cl}, respectively. The gray dashed curves indicate the migration barrier in the pristine cell. For V_{Cs}, V_{Ge}, V_{Cl}, migration barriers are estimated both in neutral and charged cells. The two bottom panels display DW migration barriers with a defect pair in the cell. The filled circles indicate the position of the point defects.

[1] Michael M. Lee, Joël Teuscher, Tsutomu Miyasaka, Takurou N. Murakami, and Henry J. Snaith. Efficient Hybrid Solar Cells Based on Meso-Superstructured Organometal Halide Perovskites. *Science*, 338(6107):643–647, 2012.

[2] Samuel D. Stranks and Giles E. Eperon and Giulia Grancini and Christopher Menelaou and Marcelo J. P. Alcocer and Tomas Leijtens and Laura M. Herz and Annamaria Petrozza and Henry J. Snaith . Electron-hole diffusion lengths exceeding 1 micrometer in an organometal trihalide perovskite absorber. *Science*, 342(6156):341–344, 2013.

[3] Loredana Protesescu, Sergii Yakunin, Maryna I. Bodnarchuk, Franziska Krieg, Riccarda Caputo, Christopher H. Hendon, Ruo Xi Yang, Aron Walsh, and Maksym V. Kovalenko. Nanocrystals of Cesium Lead Halide Perovskites ($CsPbX_3$, X = Cl, Br, and I): Novel Optoelectronic Materials Showing Bright Emission with Wide Color Gamut. *Nano Letters*, 15(6):3692–3696, 2015. PMID: 25633588.

[4] Martin A. Green, Anita Ho-Baillie, and Henry J. Snaith. The emergence of perovskite solar cells. *Nature Photonics*, 8(7):506–514, Jul 2014.

[5] Jarvist M. Frost, Keith T. Butler, and Aron Walsh. Molecular ferroelectric contributions to anomalous hysteresis in hybrid perovskite solar cells. *APL Materials*, 2(8):081506, 07 2014.

[6] Jarvist M. Frost, Keith T. Butler, Federico Brivio, Christopher H. Hendon, Mark van Schilfgaarde, and Aron Walsh. Atomistic Origins of High-Performance in Hybrid Halide Perovskite Solar Cells. *Nano Letters*, 14(5):2584–2590, 2014. PMID: 24684284.

[7] Hui-Seon Kim, Sung Kyun Kim, Byeong Jo Kim, Kyung-Sik Shin, Manoj Kumar Gupta, Hyun Suk Jung, Sang-Woo Kim, and Nam-Gyu Park. Ferroelectric Polarization in $CH_3NH_3PbI_3$ Perovskite. *The Journal of Physical Chemistry Letters*, 6(9):1729–1735, 2015. PMID: 26263341.

[8] Yasemin Kutes, Linghan Ye, Yuanyuan Zhou, Shuping Pang, Bryan D. Huey, and Nitin P. Padture. Direct observation of ferroelectric domains in solution-processed ch3nh3pbi3 perovskite thin films. *The Journal of Physical Chemistry Letters*, 5(19):3335–3339, 2014. PMID: 26278441.

[9] Bo Chen, Mengjin Yang, Shashank Priya, and Kai Zhu. Origin of J–V Hysteresis in Perovskite Solar Cells. *The Journal of Physical Chemistry Letters*, 7(5):905–917, 2016. PMID: 26886052.

[10] Ye Zhang, Eric Parsonnet, Abel Fernandez, Sinéad M. Griffin, Huaixun Huyan, Chung-Kuan Lin, Teng Lei, Jianbo Jin, Edward S. Barnard, Archana Raja, Piush Behera, Xiaoqing Pan, Ramamoorthy Ramesh, and Peidong Yang. Ferroelectricity in a semiconducting all-inorganic halide perovskite. *Science Advances*, 8(6):eabj5881, 2022.

[11] A. Nørlund Christensen and S. E. Rasmussen. A Ferroelectric Chloride of Perowskite Type. Crystal Structure of $CsGeCl_3$. *Acta Chemica Scandinavica*, 19:421–428, 1965.

[12] P. Marton, I. Rychetsky, and J. Hlinka. Domain walls of ferroelectric $BaTiO_3$ within the Ginzburg-Landau-Devonshire phenomenological model. *Phys. Rev. B*, 81:144125, Apr 2010.

[13] Ronald E. Cohen. Origin of ferroelectricity in perovskite oxides. *Nature*, 358(6382):136–138, Jul 1992.

[14] Walter J. Merz. The Electric and Optical Behavior of $BaTiO_3$ Single-Domain Crystals. *Phys. Rev.*, 76:1221–1225, Oct 1949.

[15] Marko Budimir, Dragan Damjanovic, and Nava Setter. Piezoelectric anisotropy–phase transition relations in perovskite single crystals. *Journal of Applied Physics*, 94(10):6753–6761, 11 2003.

[16] G. Shirane, H. Danner, A. Pavlovic, and R. Pepinsky. Phase Transitions in Ferroelectric $KNbO_3$. *Phys. Rev.*, 93:672–673, Feb 1954.

[17] M. Demartin Maeder, D. Damjanovic, and N. Setter. Lead Free Piezoelectric Materials. *Journal of Electroceramics*, 13(1):385–392, Jul 2004.

[18] Khuong P. Ong, Teck Wee Goh, Qiang Xu, and Alfred Huan. Structural Evolution in Methylammonium Lead Iodide $CH_3NH_3PbI_3$. *The Journal of Physical Chemistry A*, 119(44):11033–11038, 2015. PMID: 26462962.

[19] Gerhard Thiele, Heinz Wilhelm Rotter, and Klaus Dieter Schmidt. Kristallstrukturen und Phasentransformationen von Caesiumtrihalogenogermanaten(II) $CsGeX_3$ (X = Cl, Br, I). *Zeitschrift für anorganische und allgemeine Chemie*, 545(2):148–156, 1987.

[20] Li-Chuan Tang, Chen-Shiung Chang, Li-Chuan Tang, and Jung Y Huang. Electronic structure and optical properties of rhombohedral $CsGeI_3$ crystal. *Journal of Physics: Condensed Matter*, 12(43):9129, oct 2000.

[21] Debmalya Ray, Catherine Clark, Hung Q. Pham, Joshua Borycz, Russell J. Holmes, Eray S. Aydil, and Laura Gagliardi. Computational Study of Structural and Electronic Properties of Lead-Free $CsMI_3$ Perovskites (M = Ge, Sn, Pb, Mg, Ca, Sr, and Ba). *The Journal of Physical Chemistry C*, 122(14):7838–7848, 2018.

[22] Soukaina Bouhmaidi, Adil Marjaoui, Abdelali Talbi, Mohamed Zanouni, Kalid Nouneh, and Larbi Setti. A DFT study of electronic, optical and thermoelectric properties of Ge-halide perovskites $CsGeX_3$ (X=F, Cl and Br). *Computational Condensed Matter*, 31:e00663, 2022.

[23] Abduljelili Popoola, Nikhilesh Maity, Ravi Kashikar, S. Lisenkov, and I. Ponomareva. Large Electrically and Chemically Tunable Rashba–Dresselhaus Effects in Ferroelectric $CsGeX_3$ (X = Cl, Br, I) Perovskites. *The Journal of Physical Chemistry C*, 128(41):17806–17812, 2024.

[24] Beyene Tesfaw Ayalew, Shiferaw Gadisa Kuma, and Beyene Bashu Haile. Structural, electronic and transport properties of $CsGeX_3$ (X=Cl, Br, I) for energy storage and hybrid solar cell applications. *Computational Condensed Matter*, 43:e01043, 2025.

[25] Mihade El Akkel and Hamid Ez-Zahraouy. Tuning the photocatalytic performance of halide perovskites for efficient solar hydrogen production: A DFT study of $CsGeCl_{3-x}X_x$ (X= Br, I). *Solid State Communications*, 394:115721, 2024.

[26] N. F. Quackenbush, J. P. Allen, D. O. Scanlon, S. Sallis, J. A. Hewlett, A. S. Nandur, B. Chen, K. E. Smith, C. Weiland, D. A. Fischer, J. C. Woicik, B. E. White, G. W. Watson, and L. F. J. Piper. Origin of the Bipolar Doping Behavior of SnO from X-ray Spectroscopy and Density Functional Theory. *Chemistry of Materials*, 25(15):3114–3123, 2013.

[27] Dan Huang, Yu-Jun Zhao, Zhi-Ping Ju, Li-Yong Gan, Xin-Man Chen, Chang-Sheng Li, Chun mei Yao, and Jin Guo. First-principles prediction of a promising p-type transparent conductive material csgecl3. *Applied Physics Express*, 7(4):041201, mar 2014.

[28] Michael W. Swift and John L. Lyons. Lone-Pair Stereochemistry Induces Ferroelectric Distortion and the Rashba Effect in Inorganic Halide Perovskites. *Chemistry of Materials*, 35(21):9370–9377, 2023.

[29] J. Seidel, L. W. Martin, Q. He, Q. Zhan, Y.-H. Chu, A. Rother, M. E. Hawkridge, P. Maksymovych, P. Yu, M. Gajek, N. Balke, S. V. Kalinin, S. Gemming, F. Wang, G. Catalan, J. F. Scott, N. A. Spaldin, J. Orenstein, and R. Ramesh. Conduction at domain walls in oxide multiferroics. *Nature Materials*, 8(3):229–234, Mar 2009.

[30] Dennis Meier and Sverre M. Selbach. Ferroelectric domain walls for nanotechnology. *Nature Reviews Materials*, 7(3):157–173, Mar 2022.

[31] G. F. Nataf, M. Guennou, J. M. Gregg, D. Meier, J. Hlinka, E. K. H. Salje, and J. Kreisel. Domain-wall engineering and topological defects in ferroelectric and ferroelastic materials. *Nature Reviews Physics*, 2(11):634–648, Nov 2020.

[32] Mathias Schröder, Alexander Haußmann, Andreas Thiessen, Elisabeth Soergel, Theo Woike, and Lukas M. Eng. Conducting Domain Walls in Lithium Niobate Single Crystals. *Advanced Functional Materials*, 22(18):3936–3944, 2012.

[33] J. Schultheiß, J. Schaab, D. R. Småbråten, S. H. Skjærvø, E. Bourret, Z. Yan, S. M. Selbach, and D. Meier. Intrinsic and extrinsic conduction contributions at nominally neutral domain walls in hexagonal manganites. *Applied Physics Letters*, 116(26):262903, 07 2020.

[34] Didrik R. Småbråten, Quintin N. Meier, Sandra H. Skjærvø, Katherine Inzani, Dennis Meier, and Sverre M. Selbach. Charged domain walls in improper ferroelectric hexagonal manganites and gallates. *Phys. Rev. Mater.*, 2:114405, Nov 2018.

[35] Mathias Schröder, Alexander Haußmann, Andreas Thiessen, Elisabeth Soergel, Theo Woike, and Lukas M. Eng. Conducting Domain Walls in Lithium Niobate Single Crystals. *Advanced Functional Materials*, 22(18):3936–3944, 2012.

[36] D. Meier, J. Seidel, A. Cano, K. Delaney, Y. Kumagai, M. Mostovoy, N. A. Spaldin, R. Ramesh, and M. Fiebig. Anisotropic conductance at improper ferroelectric domain walls. *Nature Materials*, 11(4):284–288, Apr 2012.

[37] Tadej Rojac, Andreja Bencan, Goran Drazic, Naonori Sakamoto, Hana Ursic, Bostjan Jancar, Gasper Tavcar, Maja Makarovic, Julian Walker, Barbara Malic, and Dragan Damjanovic. Domain-wall conduction in ferroelectric $BiFeO_3$ controlled by accumulation of charged defects. *Nature Materials*, 16(3):322–327, Mar 2017.

[38] Jakob Schaab, Sandra H. Skjærvø, Stephan Krohns, Xiaoyu Dai, Megan E. Holtz, Andrés Cano, Martin Lilienblum, Zewu Yan, Edith Bourret, David A. Muller, Manfred Fiebig, Sverre M. Selbach, and Dennis Meier. Electrical half-wave rectification at ferroelectric domain walls. *Nature Nanotechnology*, 13(11):1028–1034, Nov 2018.

[39] Jill Guyonnet, Iaroslav Gaponenko, Stefano Gariglio, and Patrycja Paruch. Conduction at Domain Walls in Insulating $Pb(Zr_{0.2}Ti_{0.8})O_3$ Thin Films. *Advanced Materials*, 23(45):5377–5382, 2011.

[40] Constantinos C. Stoumpos, Christos D. Malliakas, and Mercouri G. Kanatzidis. Semiconducting Tin and Lead Iodide Perovskites with Organic Cations: Phase Transitions, High Mobilities, and Near-Infrared Photoluminescent Properties. *Inorganic Chemistry*, 52(15):9019–9038, 2013. PMID: 23834108.

[41] Jun Kang and Lin-Wang Wang. High Defect Tolerance in Lead Halide Perovskite $CsPbBr_3$. *The Journal of Physical Chemistry Letters*, 8(2):489–493, 2017. PMID: 28071911.

[42] Maksym V. Kovalenko, Loredana Protesescu, and Maryna I. Bodnarchuk. Properties and potential optoelectronic applications of lead halide perovskite nanocrystals. *Science*, 358(6364):745–750, 2017.

[43] David Cahen, Leeor Kronik, and Gary Hodes. Are Defects in Lead-Halide Perovskites Healed, Tolerated, or Both? *ACS Energy Letters*, 6(11):4108–4114, 2021.

[44] Alex M. Ganose, David O. Scanlon, Aron Walsh, and Robert L. Z. Hoye. The defect challenge of wide-bandgap semiconductors for photovoltaics and beyond. *Nature Communications*, 13(1):4715, Aug 2022.

[45] Junzhi Ye, Navendu Mondal, Ben P. Carwithen, Yunwei Zhang, Linjie Dai, Xiang-Bing Fan, Jian Mao, Zhiqiang Cui, Pratyush Ghosh, Clara Otero-Martínez, Lars van Turnhout, Yi-Teng Huang, Zhongzheng Yu, Ziming Chen, Neil C. Greenham, Samuel D. Stranks, Lakshminarayana Polavarapu, Artem Bakulin, Akshay Rao, and Robert L. Z. Hoye. Extending the defect tolerance of halide perovskite nanocrystals to hot carrier cooling dynamics. *Nature Communications*, 15(1):8120, Sep 2024.

[46] U. Schwarz, F. Wagner, K. Syassen, and H. Hillebrecht. Effect of pressure on the optical-absorption edges of $CsGeBr_3$ and $CsGeCl_3$. *Phys. Rev. B*, 53:12545–12548, May 1996.

[47] Li-Chuan Tang, Chen-Shiung Chang, Li-Chuan Tang, and Jung Y Huang. Electronic structure and optical properties of rhombohedral $CsGeI_3$ crystal. *Journal of Physics: Condensed Matter*, 12(43):9129, oct 2000.

[48] G. Kresse and J. Hafner. Ab initio molecular dynamics for liquid metals. *Phys. Rev. B*, 47:558–561, Jan 1993.

[49] G. Kresse and J. Furthmüller. Efficiency of ab-initio total energy calculations for metals and semiconductors using a plane-wave basis set. *Computational Materials Science*, 6(1):15–50, 1996.

[50] G. Kresse and J. Furthmüller. Efficient iterative schemes for ab initio total-energy calculations using a plane-wave basis set. *Phys. Rev. B*, 54:11169–11186, Oct 1996.

[51] P. E. Blöchl. Projector augmented-wave method. *Phys. Rev. B*, 50:17953–17979, Dec 1994.

[52] G. Kresse and D. Joubert. From ultrasoft pseudopotentials to the projector augmented-wave method. *Phys. Rev. B*, 59:1758–1775, Jan 1999.

[53] Aliaksandr V. Krukau, Oleg A. Vydrov, Artur F. Izmaylov, and Gustavo E. Scuseria. Influence of the exchange screening parameter on the performance of screened hybrid functionals. *The Journal of Chemical Physics*, 125(22):224106, 2006.

[54] Alejandro J. Garza and Gustavo E. Scuseria. Predicting Band Gaps with Hybrid Density Functionals. *The Journal of Physical Chemistry Letters*, 7(20):4165–4170, 2016.

[55] Benjamin G. Janesko, Thomas M. Henderson, and Gustavo E. Scuseria. Screened hybrid density functionals for solid-state chemistry and physics. *Phys. Chem. Chem. Phys.*, 11:443–454, 2009.

[56] John P. Perdew, Adrienn Ruzsinszky, Gábor I. Csonka, Oleg A. Vydrov, Gustavo E. Scuseria, Lucian A. Constantin, Xiaolan Zhou, and Kieron Burke. Restoring the Density-Gradient Expansion for Exchange in Solids and Surfaces. *Phys. Rev. Lett.*, 100:136406, Apr 2008.

[57] Alex M. Ganose, Adam J. Jackson, and David O. Scanlon. sumo: Command-line tools for plotting and analysis of periodic *ab initio* calculations. *Journal of Open Source Software*, 3(28):717, 2018.

[58] Christoph Freysoldt, Blazej Grabowski, Tilmann Hickel, Jörg Neugebauer, Georg Kresse, Anderson Janotti, and Chris G. Van de Walle. First-principles calculations for point defects in solids. *Rev. Mod. Phys.*, 86:253–305, Mar 2014.

[59] Stephan Lany and Alex Zunger. Assessment of correction methods for the band-gap problem and for finite-size effects in supercell defect calculations: Case studies for ZnO and

GaAs. *Phys. Rev. B*, 78:235104, Dec 2008.

[60] Samuel T. Murphy and Nicholas D. M. Hine. Anisotropic charge screening and supercell size convergence of defect formation energies. *Phys. Rev. B*, 87:094111, Mar 2013.

[61] Chris G. Van de Walle and Jörg Neugebauer. First-principles calculations for defects and impurities: Applications to iii-nitrides. *Journal of Applied Physics*, 95(8):3851–3879, 2004.

[62] J. Buckeridge, D.O. Scanlon, A. Walsh, and C.R.A. Catlow. Automated procedure to determine the thermodynamic stability of a material and the range of chemical potentials necessary for its formation relative to competing phases and compounds. *Computer Physics Communications*, 185(1):330–338, 2014.

[63] Graeme Henkelman, Blas P. Uberuaga, and Hannes Jónsson. A climbing image nudged elastic band method for finding saddle points and minimum energy paths. *The Journal of Chemical Physics*, 113(22):9901–9904, 2000.

[64] Graeme Henkelman and Hannes Jónsson. Improved tangent estimate in the nudged elastic band method for finding minimum energy paths and saddle points. *The Journal of Chemical Physics*, 113(22):9978–9985, 2000.

[65] U. Schwarz, H. Hillebrecht, M. Kaupp, K. Syassen, H.-G. von Schnering, and G. Thiele. Pressure-Induced Phase Transition in $CsGeBr_3$ Studied by X-Ray Diffraction and Raman Spectroscopy. *Journal of Solid State Chemistry*, 118(1):20–27, 1995.

[66] Zhi-Guang Lin, Li-Chuan Tang, and Chang-Pin Chou. Study on mid-IR NLO crystals $CsGe(Br_xCl_{1-x})_3$. *Optical Materials*, 31(1):28–34, 2008.

[67] D. J. Payne, R. G. Egdell, A. Walsh, G. W. Watson, J. Guo, P.-A. Glans, T. Learmonth, and K. E. Smith. Electronic Origins of Structural Distortions in Post-Transition Metal Oxides: Experimental and Theoretical Evidence for a Revision of the Lone Pair Model. *Phys. Rev. Lett.*, 96:157403, Apr 2006.

[68] Aron Walsh, David J. Payne, Russell G. Egdell, and Graeme W. Watson. "stereochemistry of post-transition metal oxides: revision of the classical lone pair model". *Chem. Soc. Rev.*, 40:4455–4463, 2011.

[69] Nguyen Thi Han, Vo Khuong Dien, and Ming-Fa Lin. Electronic and Optical Properties of $CsGeX_3$ (X= Cl, Br, and I) Compounds. *ACS Omega*, 7(29):25210–25218, 2022.

[70] Daniel W. Davies, Christopher N. Savory, Jarvist M. Frost, David O. Scanlon, Benjamin J. Morgan, and Aron Walsh. Descriptors for Electron and Hole Charge Carriers in Metal Oxides. *The Journal of Physical Chemistry Letters*, 11(2):438–444, 2020. PMID: 31875393.

[71] R. D. Shannon. Revised effective ionic radii and systematic studies of interatomic distances in halides and chalcogenides. *Acta Crystallographica Section A*, 32(5):751–767, Sep 1976.

[72] Zhi Deng, Yifei Mo, and Shyue Ping Ong. Computational studies of solid-state alkali conduction in rechargeable alkali-ion batteries. *NPG Asia Materials*, 8(3):e254–e254, Mar 2016.

[73] Ramaswamy Murugan, Venkataraman Thangadurai, and Werner Weppner. Fast Lithium Ion Conduction in Garnet-Type $Li_7La_3Zr_2O_{12}$. *Angewandte Chemie International Edition*, 46(41):7778–7781, 2007.

[74] Juan-Pablo Correa-Baena, Michael Saliba, Tonio Buonassisi, Michael Grätzel, Antonio Abate, Wolfgang Tress, and Anders Hagfeldt. Promises and challenges of perovskite solar cells. *Science*, 358(6364):739–744, 2017.

[75] Monojit Bag, Lawrence A. Renna, Ramesh Y. Adhikari, Supravat Karak, Feng Liu, Paul M. Lahti, Thomas P. Russell, Mark T. Tuominen, and D. Venkataraman. Kinetics of Ion Transport in Perovskite Active Layers and Its Implications for Active Layer Stability. *Journal of the American Chemical Society*, 137(40):13130–13137, 2015. PMID: 26414066.

[76] Christopher Eames, Jarvist M. Frost, Piers R. F. Barnes, Brian C. O'Regan, Aron Walsh, and M. Saiful Islam. Ionic transport in hybrid lead iodide perovskite solar cells. *Nature Communications*, 6(1):7497, Jun 2015.

[77] Kristoffer Eggestad, Benjamin A. D. Williamson, Dennis Meier, and Sverre M. Selbach. Mobile intrinsic point defects for conductive neutral domain walls in $LiNbO_3$. *J. Mater. Chem. C*, 12:17099–17107, 2024.

[78] Yi Wang, Chris Nelson, Alexander Melville, Benjamin Winchester, Shunli Shang, Zi-Kui Liu, Darrell G. Schlom, Xiaoqing Pan, and Long-Qing Chen. $bifeo_3$ domain wall energies and structures: A combined experimental and density functional theory+**U** study. *Phys. Rev. Lett.*, 110:267601, Jun 2013.

[79] B. Meyer and David Vanderbilt. Ab initio study of ferroelectric domain walls in $PbTiO_3$. *Phys. Rev. B*, 65:104111, Mar 2002.

[80] Hao-Cheng Thong, XiaoYang Wang, Jian Han, Linfeng Zhang, Bei Li, Ke Wang, and Ben Xu. Machine learning interatomic potential for molecular dynamics simulation of the ferroelectric $KNbO_3$ perovskite. *Phys. Rev. B*, 107:014101, Jan 2023.

[81] Maryam Taherinejad, David Vanderbilt, Pavel Marton, Vilgelmina Stepkova, and Jiri Hlinka. Bloch-type domain walls in rhombohedral $BaTiO_3$. *Phys. Rev. B*, 86:155138, Oct 2012.

[82] Shi Liu, Fan Zheng, Nathan Z. Koocher, Hiroyuki Takenaka, Fenggong Wang, and Andrew M. Rappe. Ferroelectric Domain Wall Induced Band Gap Reduction and Charge Separation in Organometal Halide Perovskites. *The Journal of Physical Chemistry Letters*, 6(4):693–699, 2015. PMID: 26262488.

[83] D. R. Småbråten, T. S. Holstad, D. M. Evans, Z. Yan, E. Bourret, D. Meier, and S. M. Selbach. Domain wall mobility and roughening in doped ferroelectric hexagonal manganites. *Phys. Rev. Res.*, 2:033159, Jul 2020.

[84] Greg Stone, Donghwa Lee, Haixuan Xu, Simon R. Phillpot, and Volkmar Dierolf. Local probing of the interaction between intrinsic defects and ferroelectric domain walls in lithium niobate. *Applied Physics Letters*, 102(4):042905, 01 2013.

[85] Skjærvø, Sandra H. and Småbråten, Didrik R. and Spaldin, Nicola A. and Tybell, Thomas and Selbach, Sverre M. Oxygen vacancies in the bulk and at neutral domain walls in hexagonal $YMnO_3$. *Phys. Rev. B*, 98:184102, Nov 2018.

[86] Yu Kumagai and Nicola A. Spaldin. Structural domain walls in polar hexagonal manganites. *Nature Communications*, 4(1):1540, Feb 2013.

[87] D.-K. Seo, N. Gupta, M.-H. Whangbo, H. Hillebrecht, and G. Thiele. Pressure-Induced Changes in the Structure and Band Gap of $CsGeX_3$ (X = Cl, Br) Studied by Electronic Band Structure Calculations. *Inorganic Chemistry*, 37(3):407–410, 1998. PMID: 11670288.

Supplementary Information

Defects and Domain Walls in Soft Ferroelectric $CsGeX_3$ (X = Cl, Br, I)

Kristoffer Eggestad,[1] Benjamin A. D. Williamson,[1] and Sverre M. Selbach[1]

[1] *Department of Materials Science and Engineering, NTNU - Norwegian University of Science and Technology, NO-7491 Trondheim, Norway*

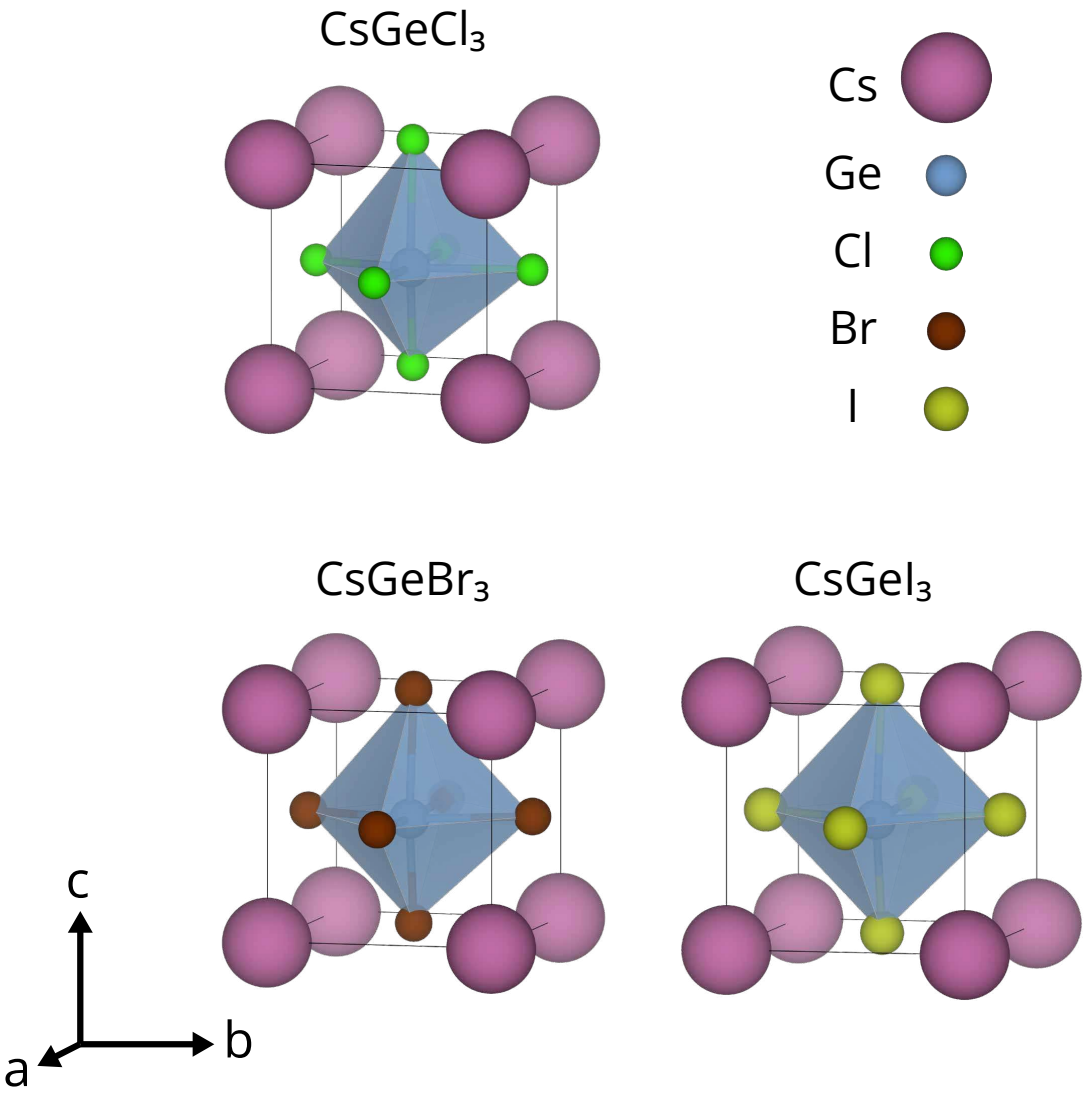

Figure S1. DFT optimised primitive structures for $CsGeCl_3$, $CsGeBr_3$ and $CsGeI_3$.

1. HSE06

SI Figure S1 shows primitive unit cells of $CsGeCl_3$, $CsGeBr_3$ and $CsGeI_3$ optimised using hybrid DFT. Lattice parameters for the primitive unit cells calculated using different functionals are compared with experimental values in Table I. In general, the HSE06 functional agrees best with experimental data and HSE06 optimised lattice parameters and atomic positions for the conventional unit cells are displayed in SI Table S1, S2, S3 and S4.

Table S1. DFT optimised lattice parameters using HSE06 for the conventional structures of $CsGeCl_3$, $CsGeBr_3$ and $CsGeI_3$.

	$CsGeCl_3$	$CsGeBr_3$	$CsGeI_3$
a, b	7.761096 Å	7.998540 Å	8.459225 Å
c	9.632980 Å	10.183176 Å	10.869453 Å
α, β	90°	90°	90°
γ	120°	120°	120°

Table S2. DFT optimised atomic positions using HSE06 for the conventional $CsGeCl_3$ structure.

Specie	a	b	c	Wyckoff
Cs	1/3	2/3	0.655318	3a
Ge	1/3	2/3	0.139602	3a
Cl	0.482434	0.964867	0.008805	9b

Table S3. DFT optimised atomic positions using HSE06 for the conventional $CsGeBr_3$ structure.

Specie	a	b	c	Wyckoff
Cs	1/3	2/3	0.662909	3a
Ge	1/3	2/3	0.13601	3a
Br	0.490037	0.980074	0.007472	9b

Calculated Bader charges, displayed in SI Table S5, show a decrease in the ionic nature of $CsGeX_3$ from the chloride to the iodide. Similar results, achieved using the PBEsol functional, are displayed in SI Table S10.

SI Table S6, S7, S8 and S9 show Born effective charges (BEC), dielectric constants, piezoelectric and elastic tensors from finite differences calculations using the HSE06 functional. The values are displayed for conventional unit cells.

Table S4. DFT optimised atomic positions using HSE06 for the conventional $CsGeI_3$ structure.

Specie	a	b	c	Wyckoff
Cs	1/3	2/3	0.666054	3a
Ge	1/3	2/3	0.133573	3a
I	0.495887	0.991775	0.007236	9b

Table S5. Bader charges calculated using the HSE06 functional.

	$CsGeCl_3$	$CsGeBr_3$	$CsGeI_3$
Cs	0.91	0.89	0.87
Ge	1.19	0.94	0.72
X	-0.70	-0.61	-0.53

Table S6. Born Effective charges (BEC) calculated using finite differences with the HSE06 functional. The BEC are displayed for the conventional unit cells.

Specie	$CsGeCl_3$	$CsGeBr_3$	$CsGeI_3$
Cs	$\begin{pmatrix} 1.38 & 0 & \\ 0 & 1.38 & 0 \\ 0 & 0 & 1.36 \end{pmatrix}$	$\begin{pmatrix} 1.44 & 0 & \\ 0 & 1.44 & 0 \\ 0 & 0 & 1.40 \end{pmatrix}$	$\begin{pmatrix} 1.46 & 0 & \\ 0 & 1.46 & 0 \\ 0 & 0 & 1.41 \end{pmatrix}$
Ge	$\begin{pmatrix} 2.97 & 0 & \\ 0 & 2.97 & 0 \\ 0 & 0 & 2.52 \end{pmatrix}$	$\begin{pmatrix} 3.36 & 0 & \\ 0 & 3.36 & 0 \\ 0 & 0 & 2.76 \end{pmatrix}$	$\begin{pmatrix} 3.81 & 0 & \\ 0 & 3.81 & 0 \\ 0 & 0 & 2.89 \end{pmatrix}$
X	$\begin{pmatrix} -1.45 & 0 & \\ 0 & -1.45 & 0 \\ 0 & 0 & -1.29 \end{pmatrix}$	$\begin{pmatrix} -1.60 & 0 & \\ 0 & -1.60 & 0 \\ 0 & 0 & -1.38 \end{pmatrix}$	$\begin{pmatrix} -1.76 & 0 & \\ 0 & -1.76 & 0 \\ 0 & 0 & -1.43 \end{pmatrix}$

Table S7. Dielectric constants for the conventional unit cells of $CsGeCl_3$,$CsGeBr_3$ and $CsGeI_3$ calculated using finite differences with the HSE06 functional.

$CsGeCl_3$	$CsGeBr_3$	$CsGeI_3$
$\begin{pmatrix} 13.63 & 0 & \\ 0 & 13.63 & 0 \\ 0 & 0 & 11.82 \end{pmatrix}$	$\begin{pmatrix} 13.85 & 0 & 0 \\ 0 & 13.85 & 0 \\ 0 & 0 & 14.86 \end{pmatrix}$	$\begin{pmatrix} 14.88 & 0 & 0 \\ 0 & 14.88 & 0 \\ 0 & 0 & 19.54 \end{pmatrix}$

Table S8. Piezoelectric tensors for the conventional unit cell calculated using finite differences with the HSE06 functional.

Material	Piezoelectric Tensor (Voigt) (C/m^2)
$CsGeCl_3$	$\begin{pmatrix} 0 & 0 & 0 & 0 & 0.32 & 0.25 \\ 0.25 & -0.25 & 0 & 0.32 & 0 & 0 \\ 0.25 & 0.25 & 0.48 & 0 & 0 & 0 \end{pmatrix}$
$CsGeBr_3$	$\begin{pmatrix} 0 & 0 & 0 & 0 & 0.41 & 0.28 \\ 0.28 & -0.28 & 0 & 0.41 & 0 & 0 \\ 0.27 & 0.27 & 0.5 & 0 & 0 & 0 \end{pmatrix}$
$CsGeI_3$	$\begin{pmatrix} 0 & 0 & 0 & 0 & 0.45 & 0.32 \\ 0.32 & -0.32 & 0 & 0.45 & 0 & 0 \\ 0.29 & 0.29 & 0.56 & 0 & 0 & 0 \end{pmatrix}$

Table S9. Elastic tensors for the conventional unit cell calculated using finite differences with the HSE06 functional.

Material	Elastic Tensor (Voigt) (GPa)
$CsGeCl_3$	$\begin{pmatrix} 22.24 & 12.26 & 9.79 & 1.57 & 0 & 0 \\ 12.26 & 22.24 & 9.79 & -1.57 & 0 & 0 \\ 9.79 & 9.79 & 16.06 & 0 & 0 & 0 \\ 1.57 & -1.57 & 0 & 7.21 & 0 & 0 \\ 0 & 0 & 0 & 0 & 7.21 & 1.57 \\ 0 & 0 & 0 & 0 & 1.57 & 4.99 \end{pmatrix}$
$CsGeBr_3$	$\begin{pmatrix} 18.38 & 10.14 & 9.16 & 2.02 & 0 & 0 \\ 10.14 & 18.38 & 9.16 & -2.02 & 0 & 0 \\ 9.16 & 9.16 & 13.13 & 0 & 0 & 0 \\ 2.02 & -2.02 & 0 & 6.33 & 0 & 0 \\ 0 & 0 & 0 & 0 & 6.33 & 2.02 \\ 0 & 0 & 0 & 0 & 2.02 & 4.12 \end{pmatrix}$
$CsGeI_3$	$\begin{pmatrix} 13.37 & 6.44 & 6.79 & 2.62 & 0 & 0 \\ 6.44 & 13.37 & 6.79 & -2.62 & 0 & 0 \\ 6.79 & 6.79 & 9.12 & 0 & 0 & 0 \\ 2.62 & -2.62 & 0 & 5.71 & 0 & 0 \\ 0 & 0 & 0 & 0 & 5.71 & 2.62 \\ 0 & 0 & 0 & 0 & 2.62 & 3.46 \end{pmatrix}$

2. PBESOL

SI Table S11, S12, S13 and S14 display born BEC, dielectric constants, piezoelectric and elastic tensors for the conventional unit cells of $CsGeCl_3$,$CsGeBr_3$ and $CsGeI_3$. BEC, piezoelectric and elastic tensors, as well as the ionic contribution to the dielectric constants, are calculated using density functional perturbation theory (DFPT) with the PBEsol functional.

Table S10. Bader charges calculated using the PBEsol functional.

Specie	$CsGeCl_3$	$CsGeBr_3$	$CsGeI_3$
Cs	0.87	0.85	0.82
Ge	1.07	0.94	0.64
X	-0.65	-0.60	-0.49

Table S11. Born Effective charges (BEC) calculated using DFPT with the PBEsol functional. The BEC are displayed for the conventional unit cells.

Specie	$CsGeCl_3$	$CsGeBr_3$	$CsGeI_3$
Cs	$\begin{pmatrix} 1.36 & 0 & \\ 0 & 1.36 & 0 \\ 0 & 0 & 1.36 \end{pmatrix}$	$\begin{pmatrix} 1.38 & 0 & \\ 0 & 1.38 & 0 \\ 0 & 0 & 1.37 \end{pmatrix}$	$\begin{pmatrix} 1.43 & 0 & \\ 0 & 1.43 & 0 \\ 0 & 0 & 1.42 \end{pmatrix}$
Ge	$\begin{pmatrix} 3.80 & 0 & \\ 0 & 3.80 & 0 \\ 0 & 0 & 3.56 \end{pmatrix}$	$\begin{pmatrix} 4.69 & 0 & \\ 0 & 4.69 & 0 \\ 0 & 0 & 4.40 \end{pmatrix}$	$\begin{pmatrix} 5.43 & 0 & \\ 0 & 5.43 & 0 \\ 0 & 0 & 4.81 \end{pmatrix}$
X	$\begin{pmatrix} -1.72 & 0 & \\ 0 & -1.72 & 0 \\ 0 & 0 & -1.64 \end{pmatrix}$	$\begin{pmatrix} -2.02 & 0 & \\ 0 & -2.02 & 0 \\ 0 & 0 & -1.92 \end{pmatrix}$	$\begin{pmatrix} -2.29 & 0 & \\ 0 & -2.29 & 0 \\ 0 & 0 & -2.08 \end{pmatrix}$

Table S12. Dielectric constants for the conventional unit cells of $CsGeCl_3$,$CsGeBr_3$ and $CsGeI_3$ calculated using DFPT with the PBEsol functional.

$CsGeCl_3$	$CsGeBr_3$	$CsGeI_3$
$\begin{pmatrix} 16.97 & 0 & 0 \\ 0 & 16.97 & 0 \\ 0 & 0 & 12.9 \end{pmatrix}$	$\begin{pmatrix} 38.07 & 0 & 0 \\ 0 & 38.07 & 0 \\ 0 & 0 & 28.86 \end{pmatrix}$	$\begin{pmatrix} 40.19 & 0 & 0 \\ 0 & 40.19 & 0 \\ 0 & 0 & 30.78 \end{pmatrix}$

Table S13. Piezoelectric tensors for the conventional unit cell calculated using DFPT with the PBEsol functional.

Material	Piezoelectric Tensor (Voigt) (C/m^2)
$CsGeCl_3$	$\begin{pmatrix} 0 & 0 & 0 & 0 & 0.68 & 0.47 \\ 0.47 & -0.47 & 0 & 0.68 & 0 & 0 \\ 0.77 & 0.77 & 0.86 & 0 & 0 & 0 \end{pmatrix}$
$CsGeBr_3$	$\begin{pmatrix} 0 & 0 & 0 & 0 & 1.03 & 0.76 \\ 0.76 & -0.76 & 0 & 1.03 & 0 & 0 \\ 1.11 & 1.11 & 1.44 & 0 & 0 & 0 \end{pmatrix}$
$CsGeI_3$	$\begin{pmatrix} 0 & 0 & 0 & 0 & 1.02 & 0.78 \\ 0.78 & -0.78 & 0 & 1.02 & 0 & 0 \\ 0.63 & 0.63 & 0.99 & 0 & 0 & 0 \end{pmatrix}$

Table S14. Elastic tensors for the conventional unit cell calculated using DFPT with the PBEsol functional.

Material	Elastic Tensor (Voigt) (GPa)
$CsGeCl_3$	$\begin{pmatrix} 20.54 & 12.74 & 12.12 & 2.4 & 0 & 0 \\ 12.74 & 20.54 & 12.12 & -2.4 & 0 & 0 \\ 12.12 & 12.12 & 16.89 & 0 & 0 & 0 \\ 2.4 & -2.4 & 0 & 6.51 & 0 & 0 \\ 0 & 0 & 0 & 0 & 6.51 & 2.4 \\ 0 & 0 & 0 & 0 & 2.4 & 3.9 \end{pmatrix}$
$CsGeBr_3$	$\begin{pmatrix} 12.82 & 6.47 & 9.93 & 2.94 & 0 & 0 \\ 6.47 & 12.82 & 9.93 & -2.94 & 0 & 0 \\ 9.93 & 9.93 & 14.86 & 0 & 0 & 0 \\ 2.94 & -2.94 & 0 & 5.26 & 0 & 0 \\ 0 & 0 & 0 & 0 & 5.26 & 2.94 \\ 0 & 0 & 0 & 0 & 2.94 & 3.18 \end{pmatrix}$
$CsGeI_3$	$\begin{pmatrix} 8.06 & 1.04 & 5.05 & 3.49 & 0 & 0 \\ 1.04 & 8.06 & 5.05 & -3.49 & 0 & 0 \\ 5.05 & 5.05 & 8.64 & 0 & 0 & 0 \\ 3.49 & -3.49 & 0 & 5.35 & 0 & 0 \\ 0 & 0 & 0 & 0 & 5.35 & 3.49 \\ 0 & 0 & 0 & 0 & 3.49 & 3.51 \end{pmatrix}$

3. ELECTRONIC STRUCTURE

SI Figure S2 and S3 show electronic DOSes and band structures calculated using the PBEsol functional. The electronic structures are similar to those calculated using the HSE06 functional (main text Figure 2 and 3), albeit show significantly smaller band gaps. SI Figure S4 displays portions of the HSE06 calculated DOSes showing the lone pair interactions together with the quantified degree of mixing of Ge_s and X_p following work by Payne et al.[1].

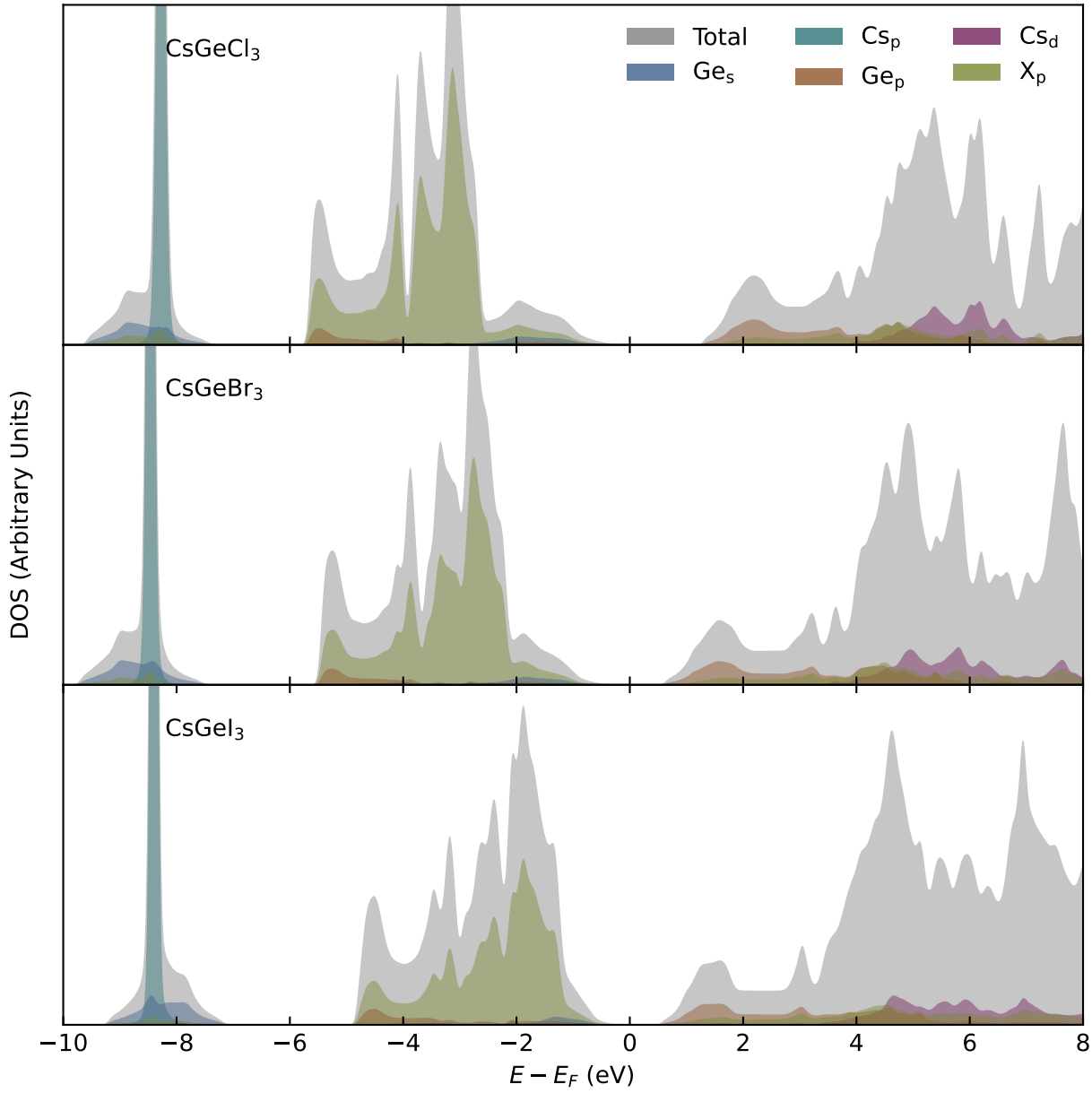

Figure S2. Electronic DOS calculated using the PBEsol functional.

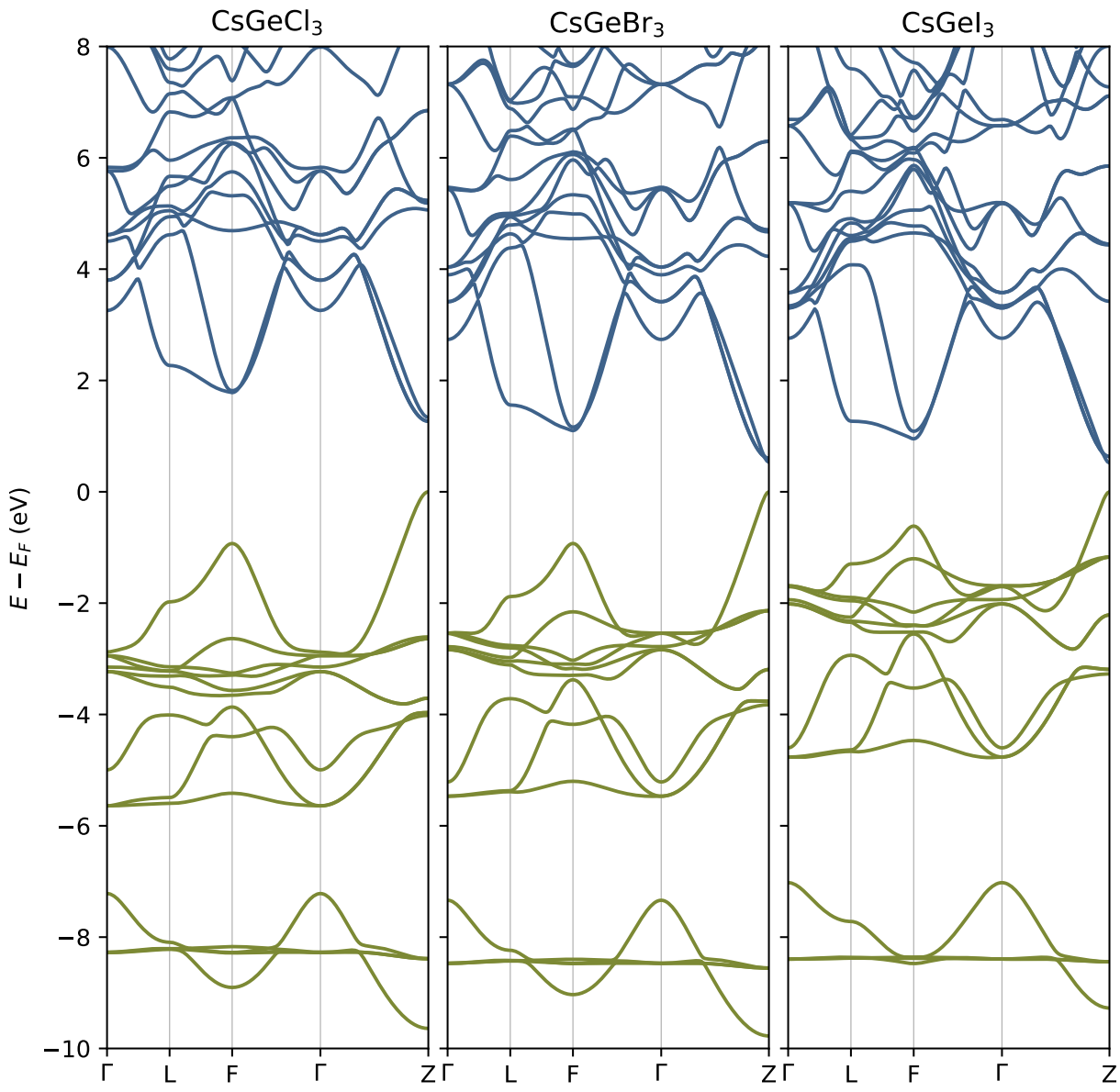

Figure S3. Electronic band structure calculated using the PBEsol functional.

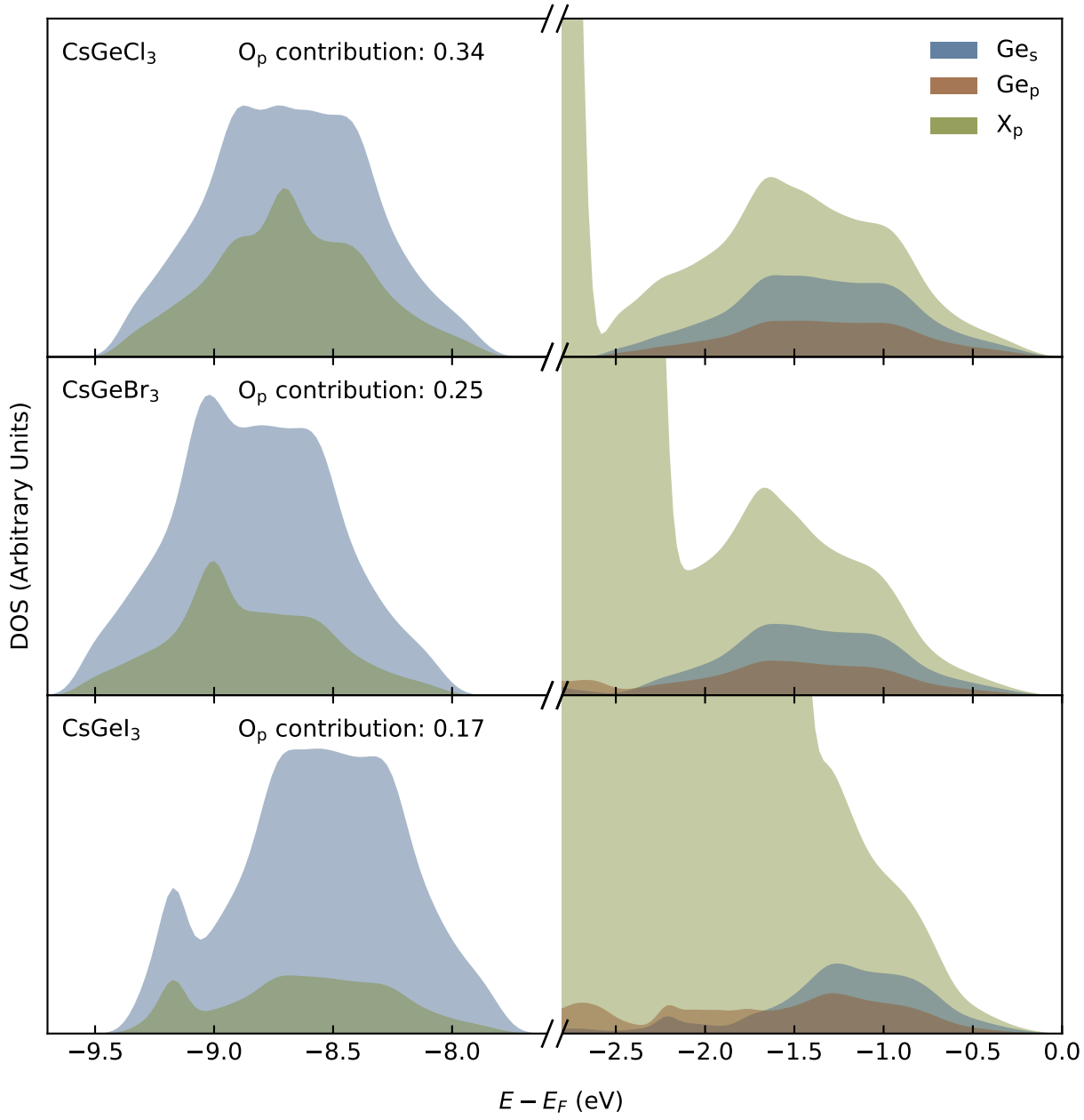

Figure S4. Electronic DOS calculated using the HSE06 functional showing the lone pair interaction.

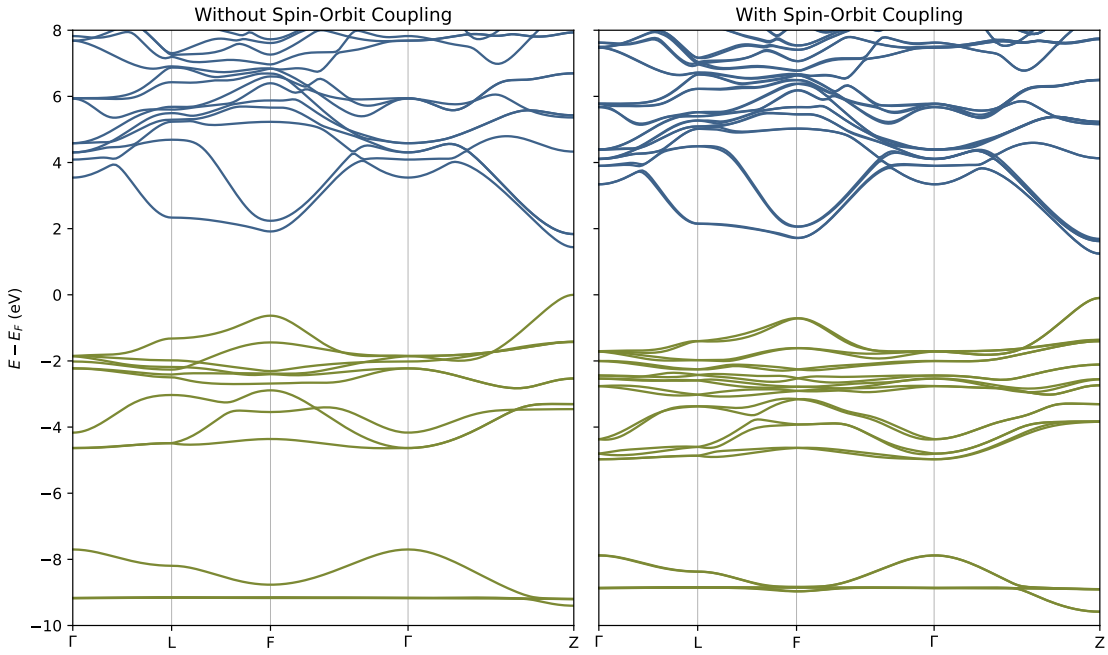

Figure S5. The band structure of $CsGeI_3$ calculated using the HSE06 functional with and without spin-orbit coupling.

4. DEFECTS

Thermodynamic stability regions for $CsGeCl_3$ and $CsGeI_3$ are shown in SI Figure S6 and S7. These are calculated by evaluating total energies of all competing phases using the Chemical Potential Limits Analysis Program (CPLAP)[2].

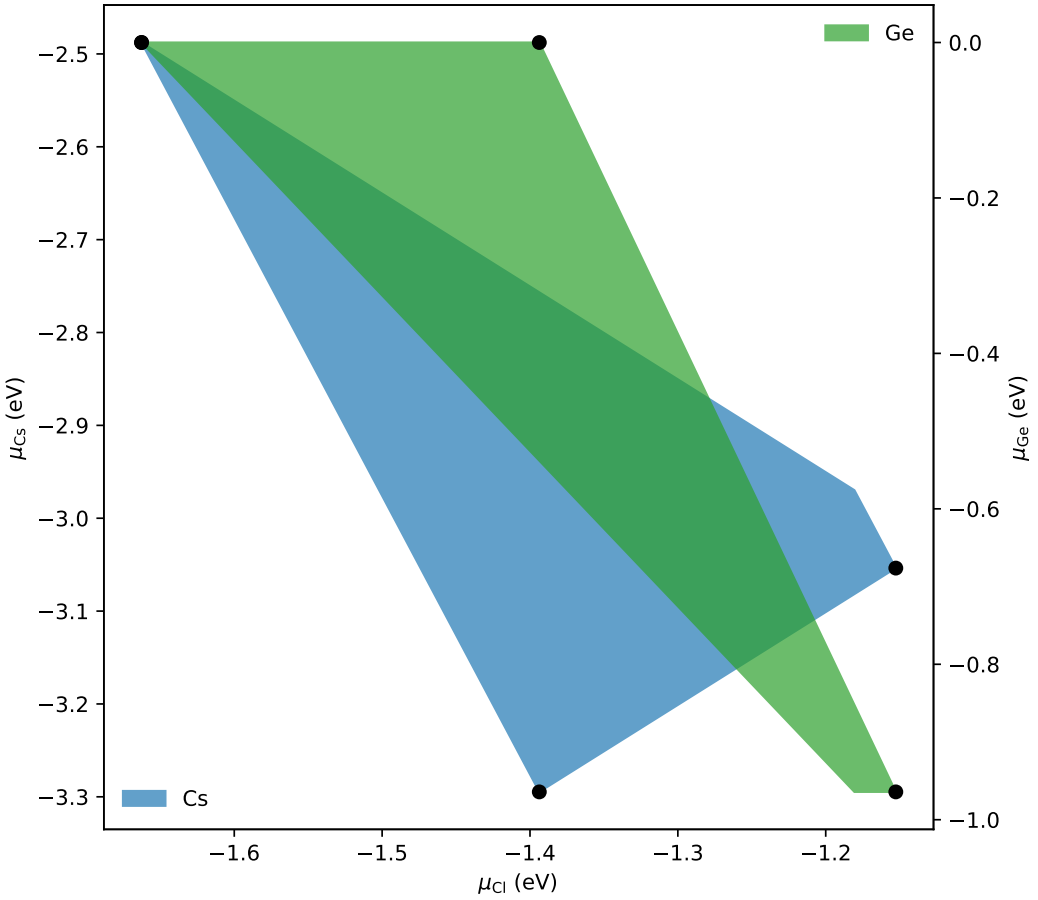

Figure S6. Thermodynamic stability region calculated using the HSE06 functional for $CsGeCl_3$. The black dots indicate the chemical potentials used in Figure 4 (a).

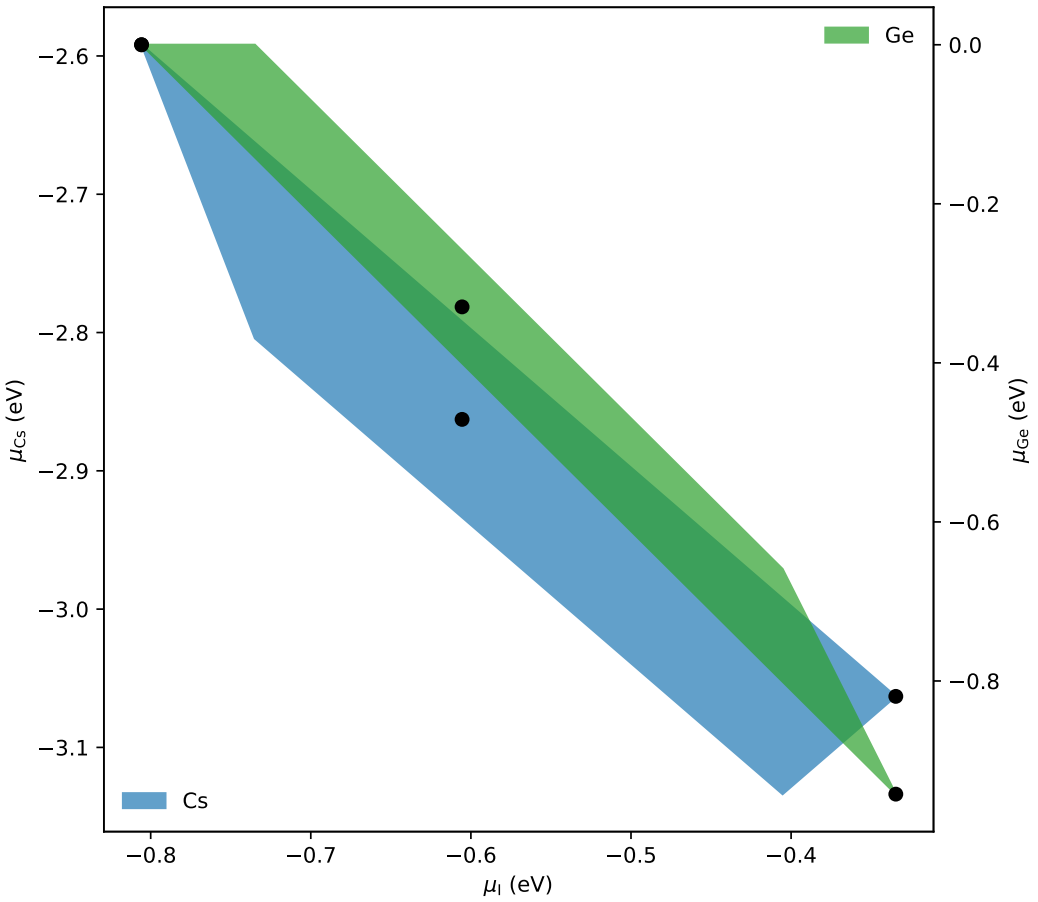

Figure S7. Thermodynamic stability region calculated using the HSE06 functional for $CsGeI_3$. The black dots indicate the chemical potentials used in Figure 4 (b).

Calculated migration barriers for V_{Cs} and V_I in $CsGeI_3$, displayed in SI Figure S8, show very similar results to V_{Cs} and V_{Cl} in $CsGeCl_3$ (main text Figure 5), indicating that halogen vacancies are very mobile in halide perovskites. SI Figure S9 show the two different halogen vacancy paths investigated. Path I is between two halogen sites with the shortest Ge-X bond to the same Ge atom, while path I is between two sites with the shortest Ge-X bond to two different Ge atoms. Path I also requires a transfer of an electron between two Ge atoms. The partial charge densities for the start and end structures of migration using path I are displayed in SI Figure S10.

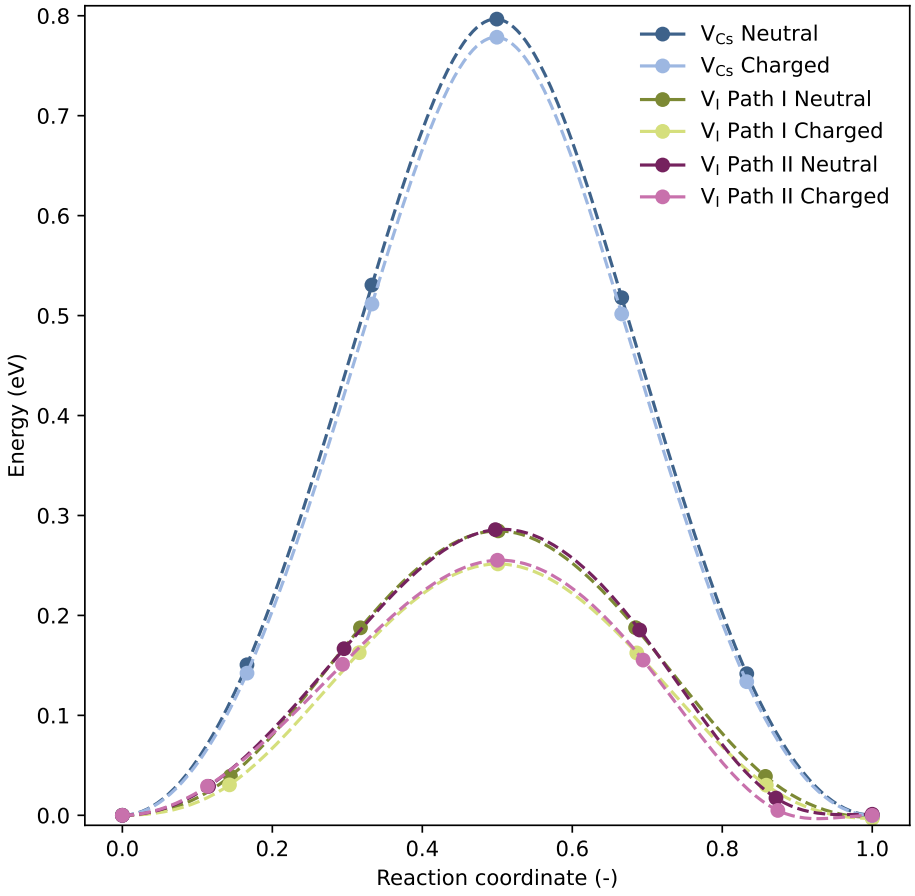

Figure S8. Migration barriers of V_{Cs} and V_I in bulk $CsGeI_3$ in charged and neutral cells calculated using the PBEsol functional.

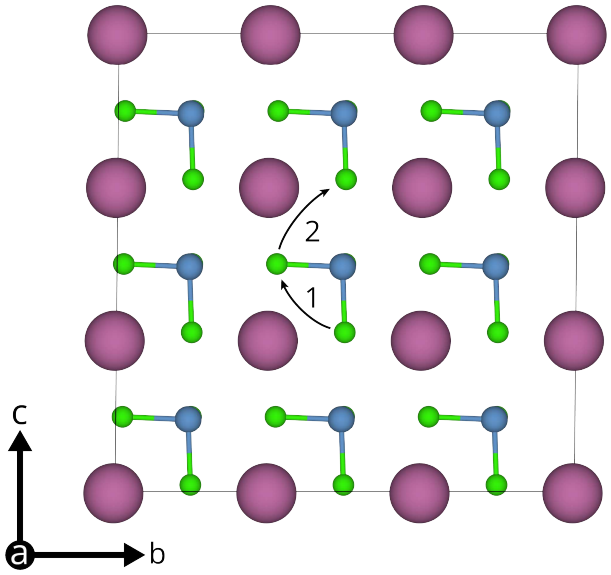

Figure S9. The two vacancy paths investigated shown in a $3 \times 3 \times 3$ supercell of $CsGeCl_3$. Only the three short bonds in each Ge-Cl octahedra are shown to make the difference between the two paths obvious.

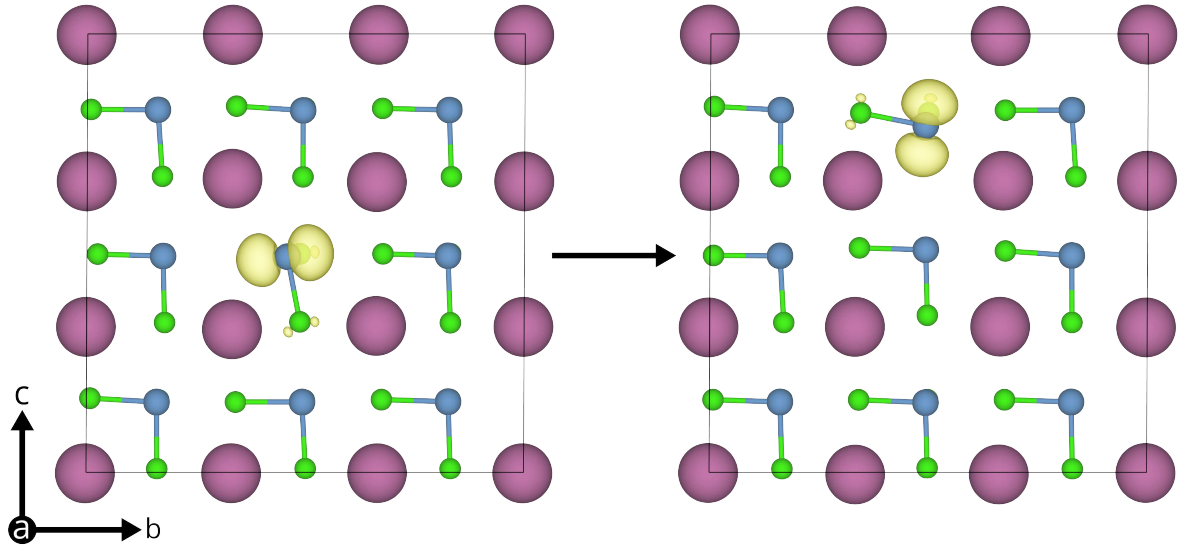

Figure S10. Partial charge density showing the charge compensating electron moving from one Ge atom to another Ge atom as a result of vacancy migration using path II.

5. DOMAIN WALLS

Table SI S15 shows how the lattice parameters for 71°, 109°, and 180° DW supercells can be calculated. a and α are the lattice parameters from the primitive cell and n determines the number of perovskites units in the supercell. Examples of the different DW supercells are displayed in SI Figure S11. The ferroelastic DWs required for the 71° and 109° DWs in $CsGeCl_3$ are not very pronounced, as the rhombohedral angle is very close to 90°.

Table S15. Formulas for calculating lattice parameters from primitive lattice parameters for 71°, 109°, and 180° Y- and X-type DW supercells.

	a'	b'	c'	α'	β'	γ'
71°	$n \cdot a \cos\frac{\alpha}{2}$	$2a \sin\frac{\alpha}{2}$	a	90°	90°	90°
109°	$n \cdot a\sqrt{1-\left(\frac{\cos\alpha}{\cos\frac{\alpha}{2}}\right)^2}$	$2a \sin\frac{\alpha}{2}$	$2a \cos\frac{\alpha}{2}$	90°	90°	90°
180° Y	$n \cdot a \sin\frac{\alpha}{2}$	a	$2a \cos\frac{\alpha}{2}$	$\arccos\frac{\cos\alpha}{\cos\frac{\alpha}{2}}$	90°	90°
180° X	$n \cdot \frac{a}{2} \cos\frac{\alpha}{2}$	$2a \cos\frac{\alpha}{2}$	$a\sqrt{3+6\cos\alpha}$	90°	90°	120°

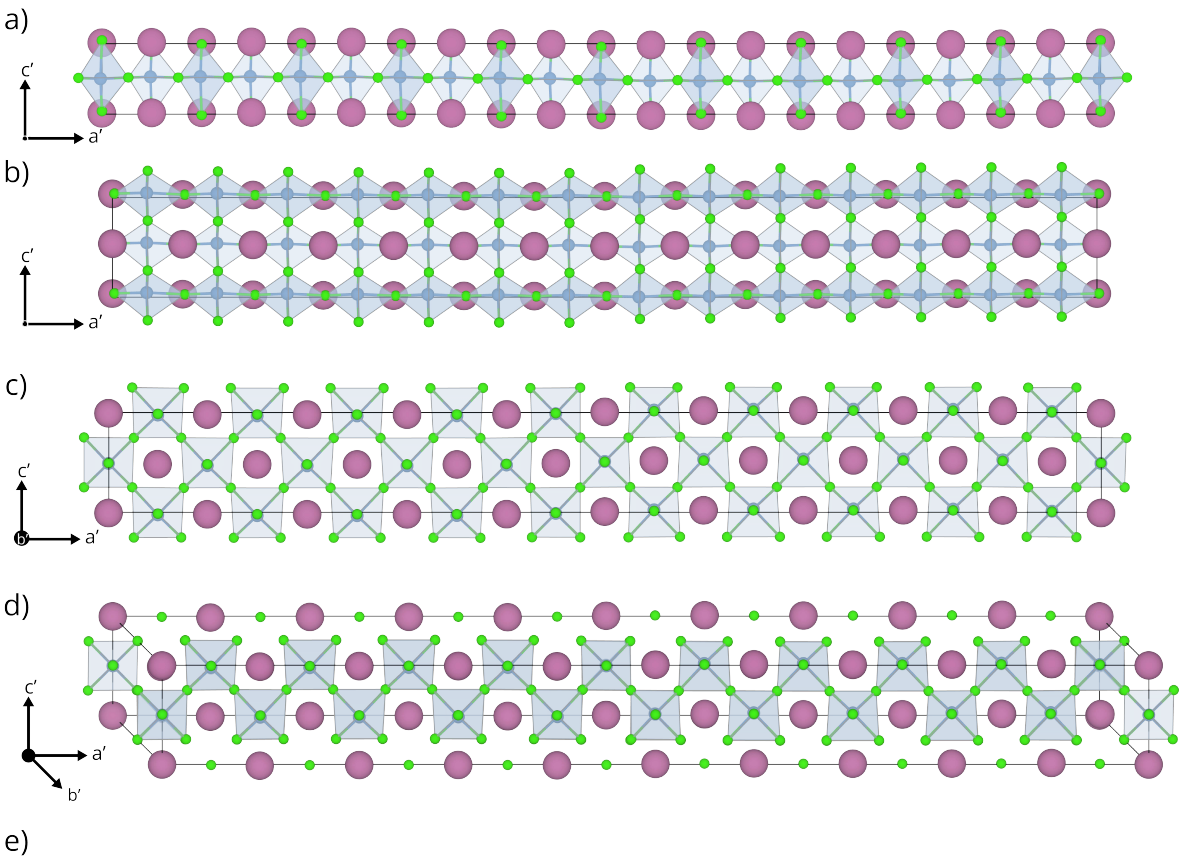

Figure S11. 71° (a), 109° (b), and 180° Y- (c) and X-type (d) DW cells for $CsGeCl_3$ optimised using the PBEsol functional.

Polarisation, calculated from formal charges, and Ge-X bond lengths as a function of distance from the DW in relaxed supercells of $CsGeCl_3$, $CsGeBr_3$ and $CsGeI_3$ are shown in SI Figure S12, S13 and S14, respectively.

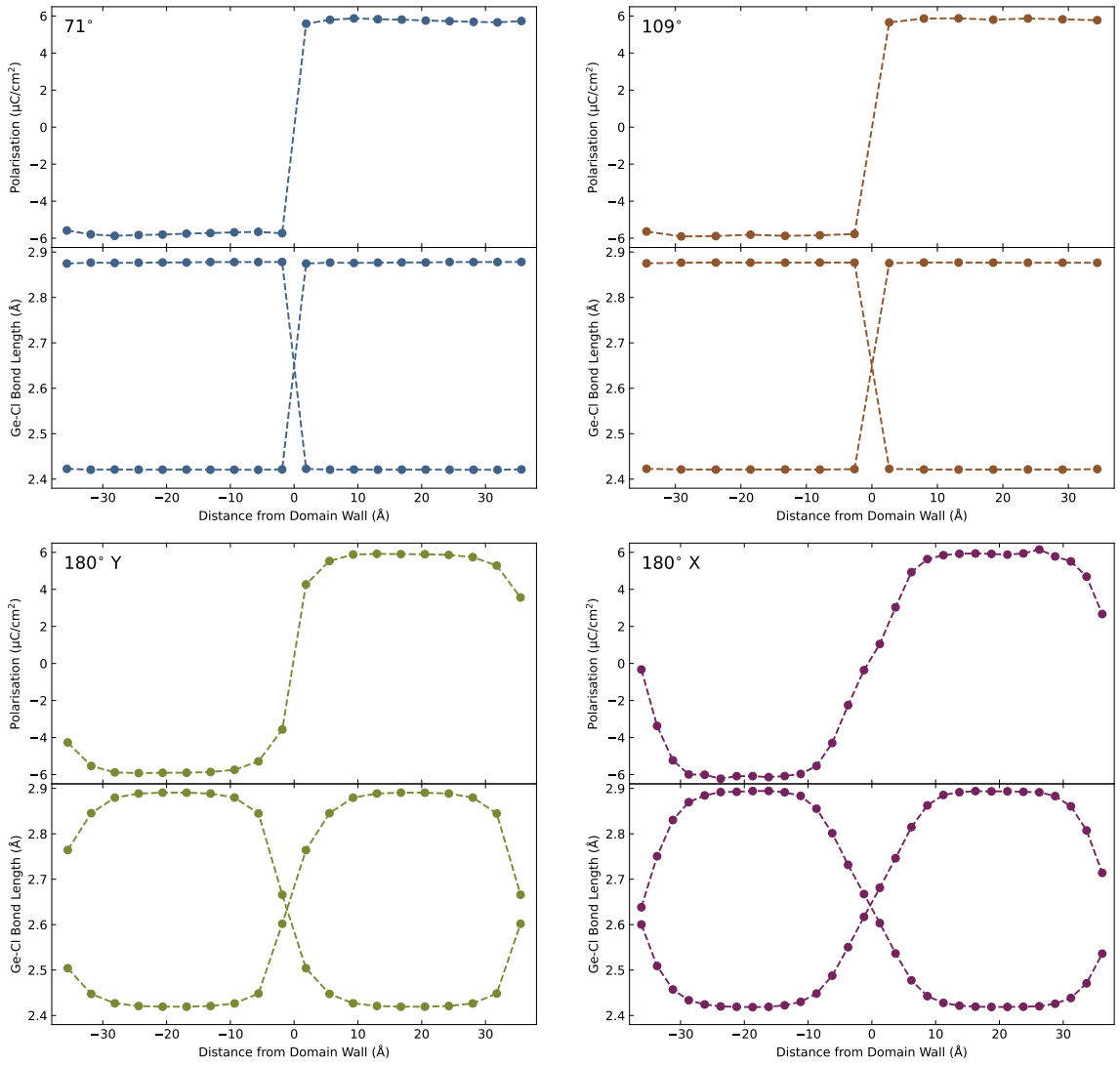

Figure S12. Polarisation and Ge-Cl distances as a function of the DW cell for 71°, 109°, and 180° Y- and X-type DWs in $CsGeCl_3$.

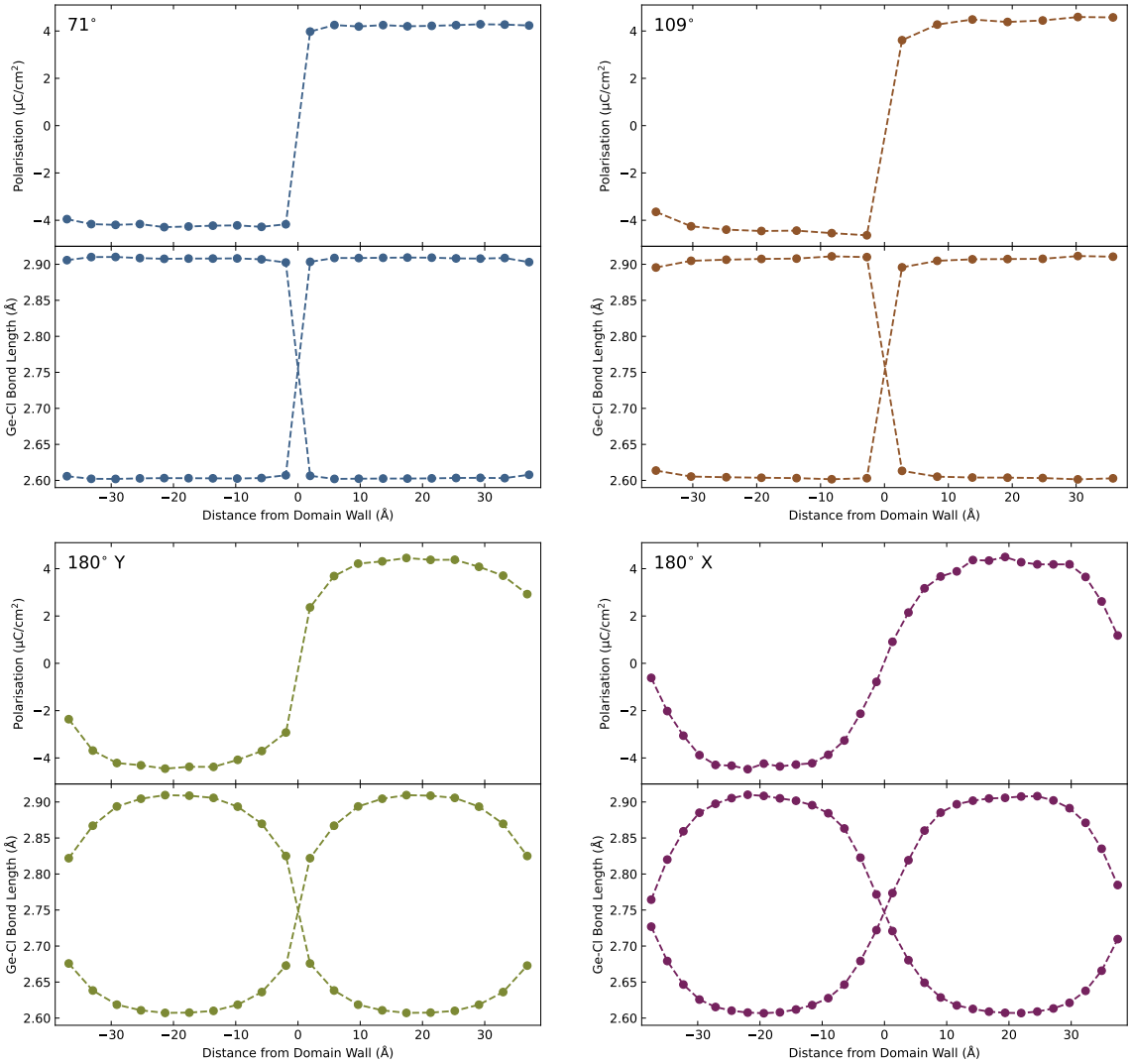

Figure S13. Polarisation and Ge-Br distances as a function of the DW cell for 71°, 109°, and 180° Y- and X-type DWs in $CsGeBr_3$.

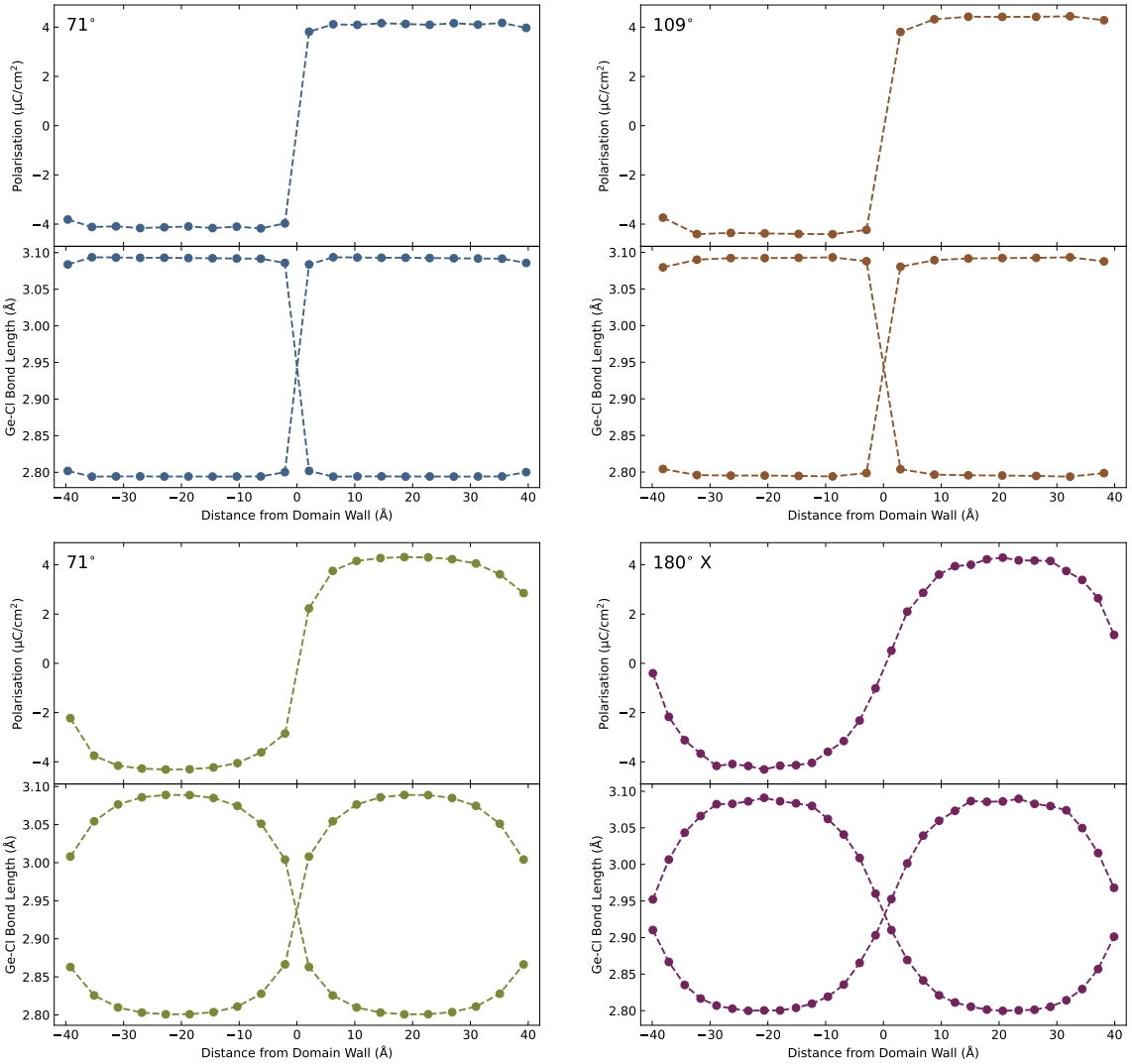

Figure S14. Polarisation and Ge-I distances as a function of the DW cell for 71°, 109°, and 180° Y- and X-type DWs in $CsGeI_3$.

SI Figure S15 shows the electronic DOS as a function of the DW cell for a 71° in $CsGeCl_3$. No visible changes to the DOS at and around the DW can be observed.

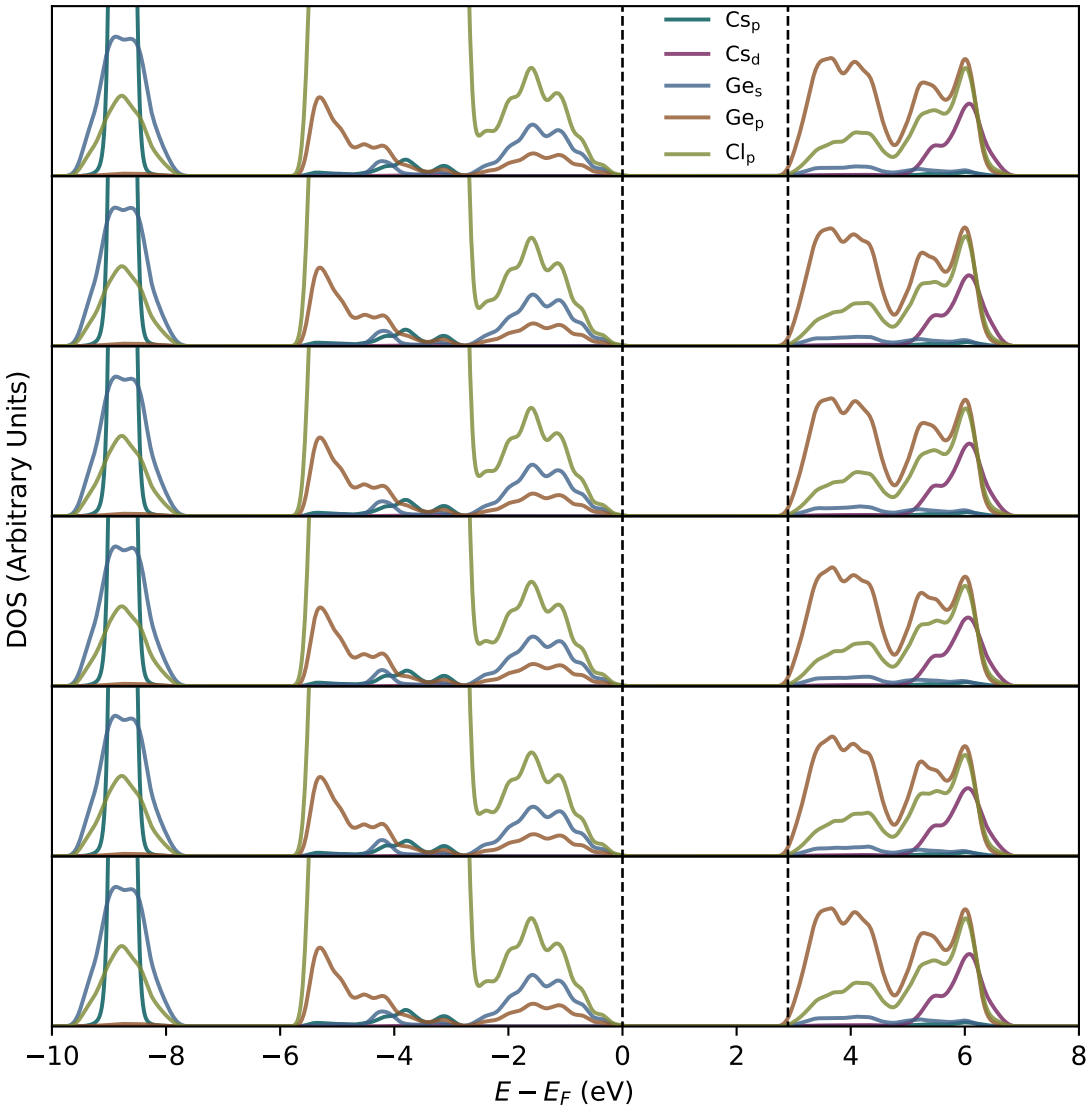

Figure S15. Layer-resolved electronic density of states for a 71° domain wall calculated using the HSE06 functional.

Normalised defect formation energies as a function of the distance to a DW are shown in SI Figure S16. The formation energies are normalised to the defect formation energy of the defect located in the middle of a domain. Most defects show a slight reduction in energy at the DW, however, the energy differences are tiny and therefore do not indicate any significant accumulation of defects at these DWs in $CsGeCl_3$.

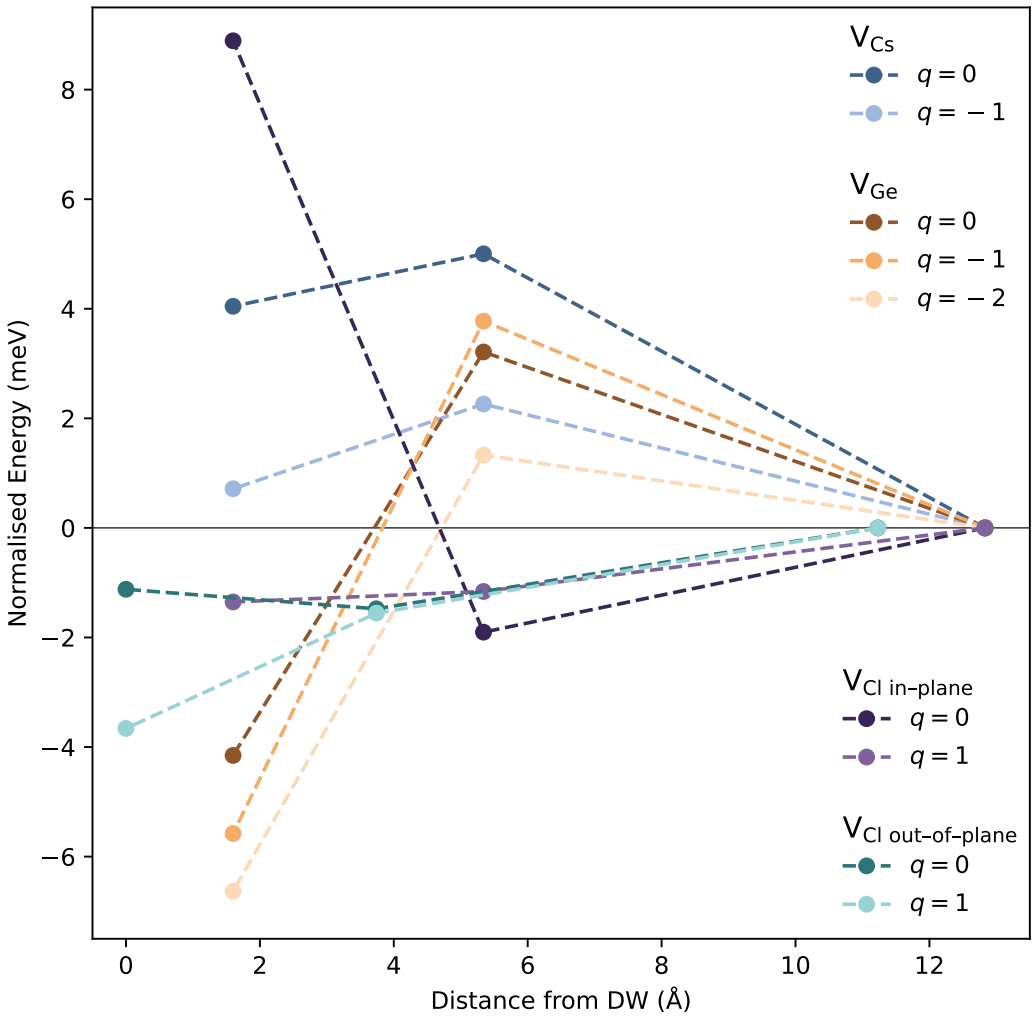

Figure S16. Normalised defect formation energies as a function of distance from a 71° DW.

The supercells used for investigations of DW pinning by point defects were created using the equations displayed in SI Table S16. A single domain unit ($n = 1$) was made by a $\begin{bmatrix} 1 & 0 & 1 \\ 1 & 2 & -1 \\ -1 & 2 & 1 \end{bmatrix}$ expansion of the primitive unit cell and displayed in SI Figure S17. As this cell does not include any ferroelastic DW, there is a very small angle between a and b×c, which is not in the DW cell created from SI Table S16.

Table S16. Formulas for calculating lattice parameters from primitive lattice parameters for the 71° DW supercell used for ci-NEB calculations with defects. n is the number of units shown in Figure S17 included.

a'	b'	c'	α'	β'	γ'
$n \cdot a\sqrt{2(1-\cos\alpha)(1+2\cos\alpha)}$	$a\sqrt{6-2\cos\alpha}$	$a\sqrt{6-2\cos\alpha}$	$\arccos\frac{1+\cos\alpha}{3-\cos\alpha}$	90°	90°

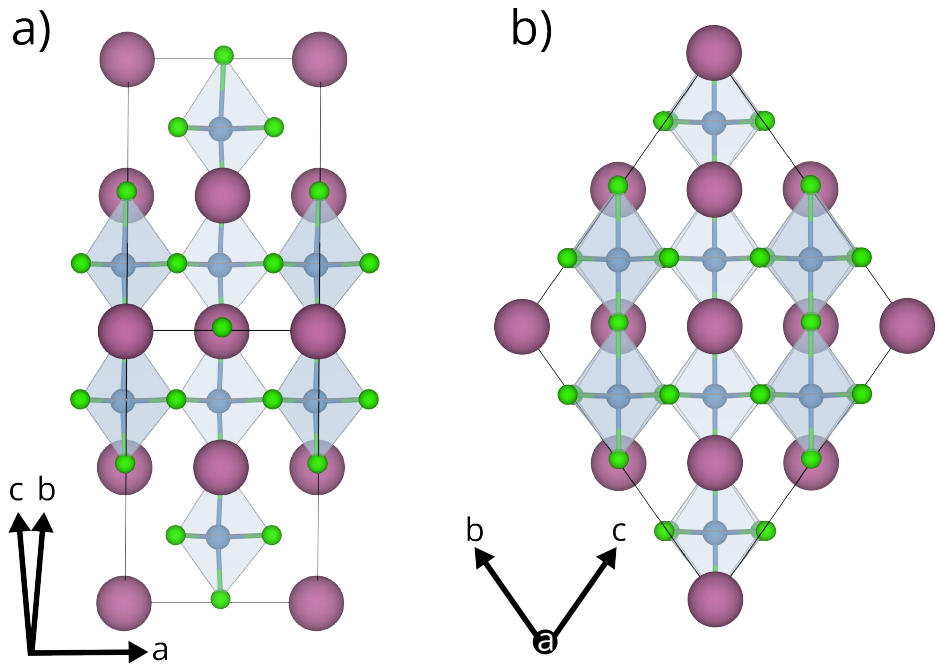

Figure S17. Visualisation of the building block ($n = 1$) used to create supercells for studying DW pinning by point defects. a) and b) is the same structure viewed from different directions.

[1] D. J. Payne, R. G. Egdell, A. Walsh, G. W. Watson, J. Guo, P.-A. Glans, T. Learmonth, and K. E. Smith. Electronic Origins of Structural Distortions in Post-Transition Metal Oxides: Experimental and Theoretical Evidence for a Revision of the Lone Pair Model. *Phys. Rev. Lett.*, 96:157403, Apr 2006.

[2] J. Buckeridge, D.O. Scanlon, A. Walsh, and C.R.A. Catlow. Automated procedure to determine the thermodynamic stability of a material and the range of chemical potentials necessary for its formation relative to competing phases and compounds. *Computer Physics Communications*, 185(1):330–338, 2014.